Early warnings of the transition to a superrotating atmospheric state

Mark S. Williamson[1,2] and Timothy M. Lenton[2]

[1]Climate Dynamics, Department of Mathematics and Statistics, Faculty of Environment, Science and Economy, University of Exeter, UK.
[2]Global Systems Institute, Faculty of Environment, Science and Economy, University of Exeter, UK.

Correspondence: Mark S. Williamson (m.s.williamson@exeter.ac.uk)

Abstract.

Several general circulation models (GCMs) have showed bifurcations of their atmospheric state under a broad range of warm climates. These include some of the more extreme global warming scenarios. This bifurcation can cause the transition to a superrotating state, a state where its angular momentum exceeds the solid body rotation of the planet. Here we use an idealized GCM to simulate this transition by altering a single non-dimensional control parameter, the thermal Rossby number. For a bifurcation induced transition there is potential for early warnings and we look for these here. Typically used early warning indicators, variance and lag 1 autocorrelation, calculated for the mean zonal equatorial wind speed, increase and peak just before the transition. The full autocorrelation function taken at multiple lags is also oscillatory, with a period of 25 days preceding the transition. This oscillatory behaviour is reminiscent of a Hopf bifurcation. Motivated by this extra structure, we use a generalised early warning vector technique to diagnose the dominant spatial modes of the horizontal windfield fluctuations. We find a zonal wavenumber zero pattern we call the 'precursor' mode, that appears shortly before and disappears soon after the transition. We attribute the increase in the early warning indicators to this spatial precursor mode.

1 Introduction

Abrupt transitions in the climate often go by the name 'tipping points' and early warnings of such tipping points are currently an active area of research (Scheffer et al., 2009; Lenton, 2011; Scheffer et al., 2012). Tipping points are loosely defined as small disturbances causing disproportionately large changes. One such example is the Atlantic meridional overturning circulation (AMOC) that can abruptly change from an 'on' to 'off' state as freshwater flux into the North Atlantic is increased (Stommel, 1961; Vellinga and Wood, 2002; Mecking et al., 2016). There are a variety of other postulated climate tipping elements including the Amazon rainforest, Greenland ice sheet and West Antarctic ice sheet. Changes in large scale atmospheric circulation patterns under anthropogenic climate change are also interesting possible candidates for tipping points. For example, there is a lively discussion on whether particular wavenumber patterns in the high latitudes are getting amplified by a 'quasi-resonance'(Mann et al., 2017) causing more frequent blocking events. The transition to an atmospheric superrotating state in warm climates is another possibly relevant tipping point that could have huge impacts if it occurred. The 3D nature of atmospheric circulation also presents interesting possibilities of novel early warning signals (EWS) of tipping points (Tantet et al., 2015). Here we look at whether there are EWS of the tipping point to superrotation in an idealised way. However, the

extension of EWS we use is more generally applicable as an approach to detecting precursors of bifurcation induced changes of state in any spatially extended or coupled system.

Mathematically tipping points can be described by (a) noise induced transitions: Probabilistic transitions between multiple steady states induced by large amplitude noise, large here meaning that the probability of a perturbation large enough to push the system into a different attractor over the timescale of interest is non-negligible. These events have limited predictability (Ditlevsen and Johnsen, 2010). (b) Rate induced transitions: These occur when the disturbance is too fast for the system to remain sitting in its current attractor resulting in a jump to a new stable state (Ashwin et al., 2012; Wieczorek et al., 2010). (c) Bifurcation induced transitions: These occur when the current stable system state loses stability, becoming unstable at the bifurcation as the disturbance (or control parameter) is slowly changed. The system will then transition to a new stable state. It is the last type, tipping due to a bifurcation, that has received the most attention as there is potential for early warnings of this sort of transition (Wiesenfeld, 1985; Held and Kleinen, 2004; Livina and Lenton, 2007; Dakos et al., 2008; Lenton et al., 2012). A bifurcation of states has been reported for the atmosphere when it transitions to a superrotating state (Suarez and Duffy, 1992; Saravanan, 1993; Shell and Held, 2004; Arnold et al., 2012; Herbert et al., 2020).

An atmospheric superrotating state is said to occur when the atmosphere rotates quicker than the planet beneath it or more precisely, the zonal angular momentum of the atmosphere exceeds the angular momentum from the solid body rotation of the planet. The solid body angular momentum per unit mass L_E at latitude θ of a planet rotating at angular velocity Ω with radius r is (see figure 1)

$$L_E = \Omega r^2 \cos^2 \theta \tag{1}$$

For a shallow atmosphere moving with zonal velocity u at latitude θ measured in the planet's rotating frame, the angular momentum per unit mass L is given by

$$L = \left(\Omega + \frac{u}{r \cos \theta} \right) r^2 \cos^2 \theta \tag{2}$$

A superrotating state occurs when $L > \max(L_E)$ for some θ. L_E is maximal at the equator ($\theta = 0$) giving $\max(L_E) = \Omega r^2$. Therefore, for a superrotating state to occur, the zonal velocity of the atmosphere u must be greater than the RHS of the following:

$$u > \Omega r \frac{\sin^2 \theta}{\cos \theta} \tag{3}$$

This condition has a minimum u at the equator ($\theta = 0$) where zonal velocity need only be positive ($u > 0$) for superrotation to occur. Moving away from the equator ($|\theta| > 0$) results in a sharp increase in zonal velocity required for superrotation. If superrotation occurs, it will almost certainly be present at the equator for a given planet. If superrotation occured at a higher latitude and not at the equator, the angular momentum increase would result in an inertially unstable atmospheric configuration. What this means for the west to east rotating planet Earth is that the prevailing easterlies at the equator ($u < 0$) change to prevailing westerlies when transitioning to superrotation. We label the bound for superrotation u_{SR} i.e.

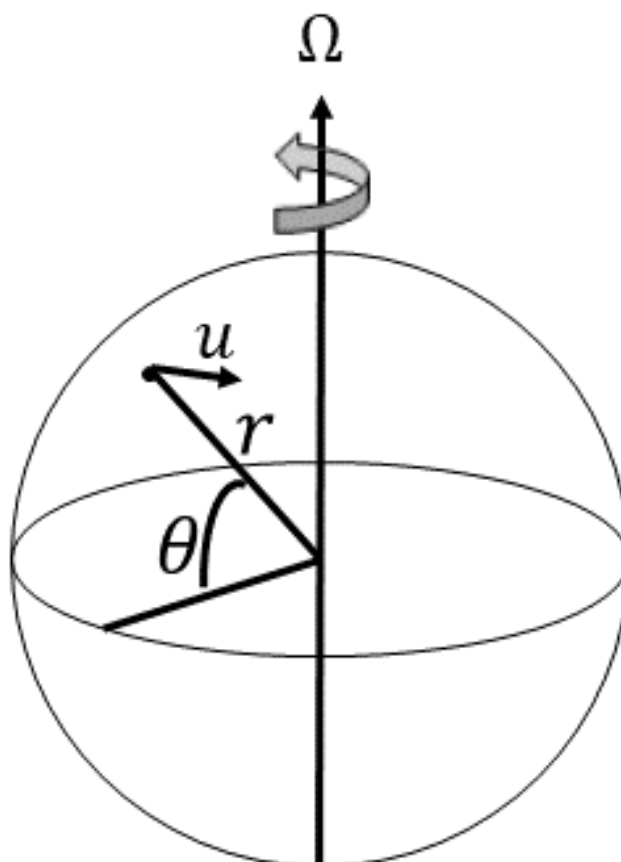$$u_{SR} = \Omega r \frac{\sin^2 \theta}{\cos \theta} \tag{4}$$

Figure 1. Schematic of the variables used to describe a superrotating atmospheric state on a planet of radius r rotating with angular velocity Ω. θ is the latitude taken relative to the equator and u is the zonal, horizontal velocity of the atmosphere in the planet's rotating frame.

Superrotating atmospheres exist on Venus and Titan (Read and Lebonnois, 2018) however they may have occurred on Earth in warmer, past climates. Caballero and Huber (2010) showed a full complexity GCM transitioned to a superrotating state when equatorial surface temperatures got sufficiently high, within the range of temperatures thought to have existed in the early Cenozoic period of Earth history, 65 million years ago. This was a period where it was around 10°C warmer on average than today. The atmospheres of other warmer periods such as the early Pliocene and Eocene may also have been superrotating (Tziperman and Farrell, 2009). Simulations of warm climates that generate enhanced tropical convective variability seem particularly prone to superrotation (Arnold et al., 2012) as do those where convective heating strengthens (Laraia and Schneider, 2015). This has led to the hypothesis that it may be relevant to future climate projections (Held, 1999; Pierrehumbert, 2000) and account for the superrotation seen in extreme global warming simulations (Huang et al., 2001). Even though the probability of

transitioning to a superrotating state is presently thought to be low as the Earth warms into the future (Caballero and Carlson, 2018), the possibility is high risk - for example, if the prevailing Pacific equatorial westerlies switched to the easterlies of an atmosphere with superrotation at the surface, a permanent El Nino state would result and with it, all the global impacts that
70 entail (Pierrehumbert, 2000). Tziperman and Farrell (2009) used this mechanism to explain the permanent El Nino state that is thought to have existed in the Pliocene.

Transitions to superrotating states may be smooth (Huang et al., 2001; Caballero and Huber, 2010; Mitchell and Vallis, 2010) or abrupt (Suarez and Duffy, 1992; Saravanan, 1993; Arnold et al., 2012). The smooth, gradual type seem to be more common in simulations of global warming scenarios or warm paleoclimates with comprehensive, multilevel GCMs (Arnold
75 et al., 2012). Abrupt transitions are seen more commonly in models with some degree of idealisation, however that is not rule them out in realistic scenarios (Held, 2016). The original example of an abrupt transition to a superrotating state was found by Suarez and Duffy (1992) in a two layer GCM as the tropical heating was increased. This transition also showed hysteresis - that is as the tropical heating was reversed below the transition's critical value, the superrotating state persisted to a new and lower critical value. Arnold et al. (2012) have found similar behaviour in a higher resolution, multilevel, although still idealised
80 GCM. This bistability is something we will also investigate in a different setting in this manuscript.

Tipping points and bifurcation induced transitions are often, but not necessarily, abrupt (Armstrong McKay et al., 2022; Strogatz, 2001). The transition to superrotation reported here is smooth. Nevertheless, early warnings of the transition are shown and therefore these simulations serve as a test bed for whether we can detect this transition before it happens.

In this manuscript the focus will be the fluctuations around the mean wind field state and how their properties change as the
85 atmosphere gets closer to a superrotating state, the idea being that these properties can serve as early warnings of the transition. We first introduce the idealised GCM used for these numerical simulations in section 2 as well as the control parameter we vary to span Earth-like to fully rotating atmospheric states. We then describe this range of simulated mean atmospheric states in section 3 before going to the main focus of the manuscript, early warnings of the transition. We start by calculating the widely used early warning indicators in section 4. Motivated by the bistability in the superrotating states observed in the experiments of
90 Suarez and Duffy (1992) and others, we look for bistability with our control parameter in section 5. In section 6, we generalise the usual early warning indicators to the vector setting. This allows us to diagnose the dominant spatial patterns in the wind field fluctuations preceding the superrotation transition as well as the dominant patterns following the transition. We discuss and conclude in section 7.

2 Methods

95 We use an idealized general circulation model (GCM) to simulate the transition to superrotation. The model framework we use is Isca (Vallis et al., 2018) which is based on a spectral dry dynamical core obeying the primitive equations of motion of Gordon and Stern (1982). Isca is designed to be highly configurable for use in exoplanet research both in complexity (multiple radiation schemes and moist/dry atmospheres are options) and parameter values (planetary radius, rotation rate, fluid density are among the many that can be altered). The configuration we use here is as simplified as possible and follows the approach

100   of Mitchell and Vallis (2010) closely. Simulations are performed at T42 resolution (about 2.8^o resolution at the equator) and

with 25 vertical sigma levels (equal pressure levels $\sigma = p/p_s$ where p is pressure and p_s is surface pressure).

The surface of the planet is prescribed to be isotropically smooth with no topography or continents present. No radiation

scheme is used either. Instead temperature is linearly relaxed to a prescribed mean annual average state (Newtonian cooling)

using the scheme of Held and Suarez (1994). In particular, the surface temperature is relaxed to the zonally symmetric profile

105     $$T_0 = \overline{T}[1 + \frac{\Delta_H}{3}(1 - 3\sin^2\theta)] \tag{5}$$

with T_0 being the lowest level temperature and $\overline{T}$ the global average surface temperature. Δ_H is a non-dimensional parameter

specifying the pole to equator temperature difference. The vertical temperature is assumed to relax to a moist adiabat with lapse

rate 6 K km^{-1} capped at a minimum of 200 K in the stratosphere. The radiative relaxation time is 40 days in free troposphere

and approximately 4 days in the boundary layer, the top of which is fixed at $p/p_0 = 0.7$ (see Held and Suarez (1994) for

110   the full functional forms). As previously mentioned we follow Mitchell and Vallis (2010) closely although there are some

minor differences: Mitchell and Vallis (2010) use $\overline{T} = 315$ K and $\Delta_H = 0.2$, here we use $\overline{T} = 314$K and $\Delta_H = 0.215$. As both

of these parameters combine together in a non-dimensional number that will be used as the control parameter in numerical

experiments (the thermal Rossby number, see below) these small differences should be negligible in comparing our results

with theirs.

115   Friction from the planet's surface on the atmosphere acts as a negative source of angular momentum in the atmospheric

boundary layer and this is specified as a linear, vertical height dependent (Rayleigh) drag on the horizontal velocities given by

$$\frac{\partial \mathbf{v}}{\partial t} = -k_v(\sigma)\mathbf{v} \tag{6}$$

$$k_v(\sigma) = k_f \max\left(0, \frac{\sigma - \sigma_b}{1 - \sigma_b}\right) \tag{7}$$

where $\mathbf{v}$ is a vector of the horizontal velocities $:= (u, v)$. The reciprocal of the Rayleigh relaxation time, k_f, is taken to be 1/2

120   day^{-1} at the planet surface ($\sigma = 1$) and linearly decreases to zero at the top of the boundary layer at $\sigma_b = 0.7$. This is slightly

smaller than the value of 1 day^{-1} used in Mitchell and Vallis (2010).

The horizontal momentum equations governing the atmospheric dynamics simplify in non-dimensional form when subject

to Rayleigh friction and Newtonian cooling. These equations are then governed by just a few non-dimensional parameters.

The relevant non-dimensional parameter that is varied in the experiments here and in Mitchell and Vallis (2010) is the thermal

125   Rossby number

$$Ro_T = \frac{RT_0\Delta_H}{(2\Omega r)^2} \tag{8}$$

R here is the specific gas constant for dry air (287 J K^{-1} kg^{-1}). As the numerical model code is dimensional however, a

dimensional parameter must be varied and this is chosen to be the planetary radius r. By making this choice the other non-

dimensional parameters, the Ekman number and thermal relaxation time, remain unaltered.

130   To summarise, in the following experiments we vary the thermal Rossby number to go from Earth like atmospheric states

($Ro_T = 0.02$) through the transition ($Ro_T \sim 1$) to a fully superrotating states ($Ro_T > 1$) by changing the planetary radius r

for each simulation. All other parameters will remain fixed. Each simulation is initialized from a homogenous atmospheric state and integrated for 3 years (1080 days). A stationary state is reached after approximately 200 days. However, in the results following we only use the last two years of the three year simulation to ensure the model is in equilibrium.

135 ## 3   Mean atmospheric state with varying Ro_T

In figure 2 we show the zonal time mean windspeed u with latitude θ and height $\sigma = p/p_s$ after the atmosphere has reached a stationary state (the last two years of a three year integration). Three different values of Ro_T are presented corresponding to an Earth-like atmospheric state ($Ro_T = 0.02$), a state close to the superrotation transition ($Ro_T = 0.87$) and a fully superrotating state ($Ro_T = 11.39$). The zero contour ($u = 0$) is shown as the black line, $u < 0$ are blue contours and $u > 0$ are red. Focussing

140 on the equatorial region ($\theta = 0$), no superrotation at any vertical level is present in the Earth-like simulation (black contours mark the edge of the red, potentially superrotating $u > 0$ regions either side of the equator). Superrotation is present at $Ro_T = 0.87$ above the height of the boundary layer ($\sigma = 0.7$) but absent within it. In the $Ro_T = 11.39$ simulation, superrotation occurs within the boundary layer but at heights above $\sigma = 0.8$. Superrotation is more likely to be found at all vertical levels at the equator as Ro_T increases. Other notable features are the mid-latitude jets in the Earth-like simulation centred at $\sigma \sim 0.3$ and at

145 latitude $\theta \sim \pm 50^o$. These jets move poleward as Ro_T increases.

None of the simulations show superrotation ($u > 0$) at the equator in the lowest two vertical levels ($\sigma > 0.8$). This is due to Rayleigh drag within the boundary layer ($\sigma \geq 0.7$) decelerating the horizontal flow and acting as a negative angular momentum flux. For superrotation to occur there must be a time integrated positive flux of momentum into the equatorial region that exceeds the time integrated negative flux from the Rayleigh drag. With the drag parameterization used, this is only possible for

150 the third vertical level in the model and higher ($\sigma < 0.8$). We exclusively study the wind speeds in the lowest vertical level that shows superrotation from here on (the third vertical level $\sigma = (0.7\ 0.79]$ with mid point $\sigma = 0.74$). This level is still inside the atmospheric boundary layer and so still experiences a small amount of drag however positive momentum sources can exceed it for a range of Ro_T. This level lies roughly at a vertical height of $\sim$ 2 - 3 km above sea level.

In figure 3 we show the zonal mean wind speed (black line) with latitude θ at the third vertical level ($\sigma = 0.74$) for a range

155 of Ro_T along with the minimal u required for superrotation as a function of latitude (red line, equation 4). The threshold for superrotation at the equator occurs roughly at $Ro_T \sim 1$. For values of $Ro_T > 1$ there are regions around the equator where the black line lies above the red line threshold indicating the presence of superrotation.

We also show snapshots ($t = 900$ days into the simulation) of the horizontal wind field ($\mathbf{v} = (u, v)$) at this vertical level ($\sigma = 0.74$) for three different values of Ro_T in figure 4. The midlatitude instabilities are evident in the $Ro_T = 0.02$ simulation

160 and lack of superrotation at the equator (blue colour). The sign of the zonal velocity is patchy at the equator close to the transition ($Ro_T = 0.87$) and fully positive signifying superrotation in the $Ro_T = 11.39$ simulation.

More information on the mean states and the mechanisms of superrotation in these simulations is reported in Mitchell and Vallis (2010). From here on we get to the main focus of this manuscript, namely we study the fluctuations around the mean states and their properties as precursors to the transition.
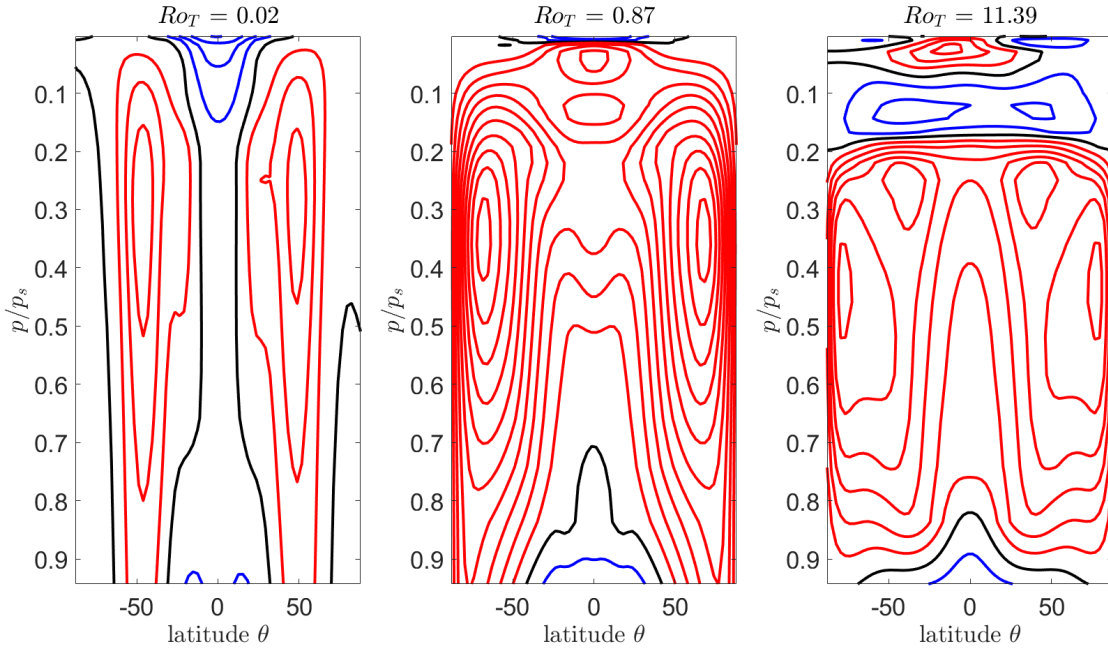
Figure 2. Vertical and zonal structure of mean u state: Zonal mean u with latitude and vertical height $\sigma = p/p_0$. $u > 0$ contours are shown in red, $u = 0$ contour is black and $u < 0$ are blue. An Earth-like state is shown on the LHS ($Ro_T = 0.02$), a state close to the superrotation transition (middle plot, $Ro_T = 0.87$) and a fully superrotating state is shown on the RHS ($Ro_T = 11.39$).

4 Temporal early warning signals

In this section we calculate early warning signals (EWS) for the varying Ro_T simulations with the aim of early detection of the transition to a superrotating state. These indicators are widely used to detect abrupt transitions resulting from local bifurcations (Lenton, 2011; Thompson and Sieber, 2011). Typically, these are designed to detect the increasing recovery time and amplitude of small fluctuations $\delta x(t)$ around the mean, stationary state denoted $\overline{x}$ of some scalar state parameter $x(t)$ that is a function of time t. The state of the system is therefore given by

$$x(t) = \overline{x} + \delta x(t) \tag{9}$$

and is often assumed to evolve autonomously according to some function $f(x)$ as $\dot{x} = f(x)$ (overdots denote ordinary time derivatives i.e. $\dot{x} := \frac{dx}{dt}$). $f(x)$ is a nonlinear function of x in general. Provided the fluctuations are not too large, one can approximate the dynamics well by Taylor expanding $f(x)$ to first order around the mean state i.e. $f(x) \approx f(\overline{x}) + J(\overline{x})\delta x$ where the Jacobian is given by $J(\overline{x}) = \frac{\partial f(x)}{\partial x}|_{x=\overline{x}}$. In this case the dynamics of the fluctuations can be approximated with a linear first order ordinary differential equation (ODE) i.e.

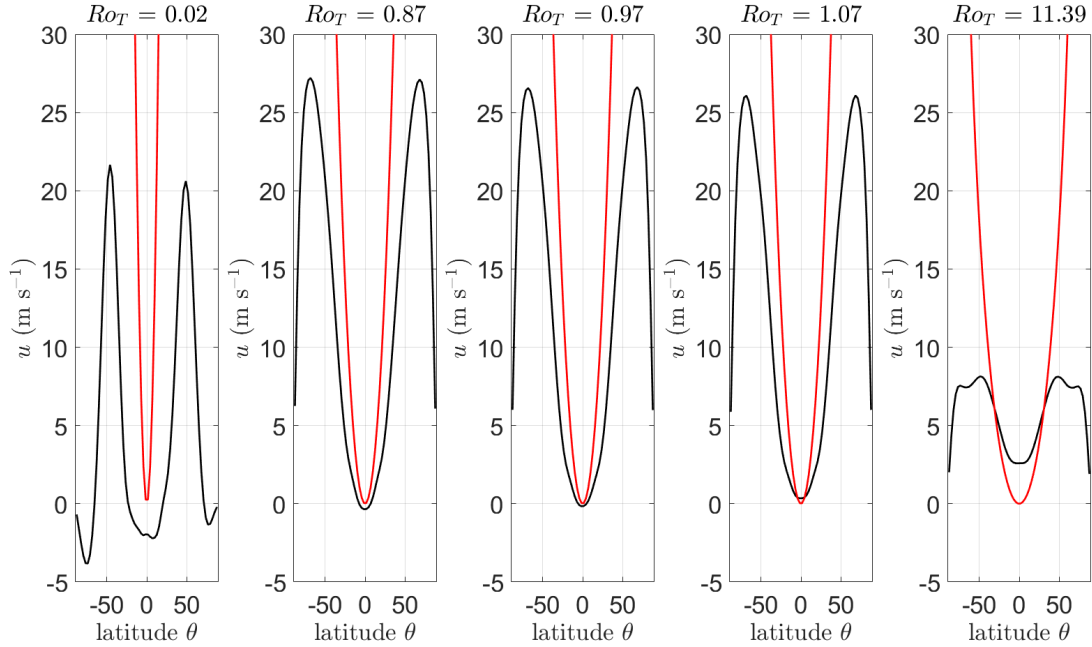$$\dot{\delta x} \approx J(\overline{x})\delta x \tag{10}$$

7

Figure 3. Zonal structure of mean u state at fixed height: Zonal mean u (black line) with latitude θ at vertical level $\sigma = 0.74$ for a range of thermal Rossby numbers (Ro_T) from Earth like ($Ro_T = 0.02$) to fully superrotating ($Ro_T = 11.39$). The middle three panels are small increments through the transition at $Ro_T \sim 1$. The red line is the minimal u required for superrotation at that latitude. The superrotation threshold is reached at $Ro_T \sim 1$ at the equator.

For a time invariant mean state $\overline{x}$ (and time invariant $J(x)$) this simple ODE has the solution

$$\delta x(t) = e^{J(\overline{x})t} \delta x(0). \tag{11}$$

180 There are three possible fates of an initial fluctuation of amplitude $\delta x(0)$ depending on the sign of the real part of $J(\overline{x})$: (i) The real part of $J(\overline{x})$ is negative ($\mathcal{R}(J(\overline{x})) < 0$); the initial fluctuation $\delta x(0)$ decays and the system state will be stable to perturbations eventually recovering to $\overline{x}$. In this case a recovery, or e folding time can be defined as the time taken, τ, for the fluctuation to reach $1/e$th of its initial value as $\tau = -1/\mathcal{R}(J(\overline{x}))$. (ii) The real part of $J(\overline{x})$ is positive ($\mathcal{R}(J(\overline{x})) > 0$); any initial fluctuation will get exponentially larger with time and the system will not recover to $\overline{x}$ i.e. $\overline{x}$ is unstable. (iii) The real

185 part of $J(\overline{x})$ is zero i.e. $\mathcal{R}(J(\overline{x})) \to 0$. In this case, perturbations will not grow or decay. This neutral stability occurs at a bifurcation.

Early warning indicators are designed to detect the increasingly less negative value of $\mathcal{R}(J(\overline{x}))$ or equivalently the increasing system recovery time τ as it approaches the bifurcation. This phenomenon is termed 'critical slowing down'. One popular indicator is the variance σ_x^2 of x with time

190 $$\sigma_x^2 = E[(x(t) - \overline{x})^2] \tag{12}$$

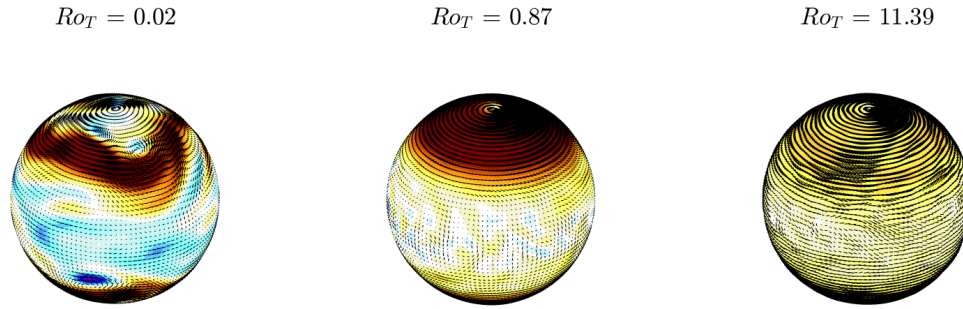$$Ro_T = 0.02 \qquad\qquad Ro_T = 0.87 \qquad\qquad Ro_T = 11.39$$

Figure 4. Snapshots of the horizontal $\mathbf{v} = (u, v)$ wind field at vertical level $\sigma = 0.74$ (vectors) at $t = 900$ days for a range of thermal Rossby numbers (Ro_T). The colour plot is the u component with red colours showing $u > 0$ and blue colours showing $u < 0$. LH panel shows an Earth-like mean state, middle panel is the mean state just before the transition to superrotation and RH panel shows a fully superrotating mean state.

$$= E[\delta x(t)^2] \tag{13}$$

where $E[.]$ is the expectation value. For the case where x is a scalar variable with first order dynamics subject to random (white noise) forcing, $J(x)$ is also a real scalar and the variance is given by

$$\sigma_x^2 = \frac{\sigma_Q^2}{2|J(\overline{x})|} \tag{14}$$

195 This measures the mean amplitude of the system fluctuations σ_x to a random mean forcing of size σ_Q (σ_Q is generally assumed to be constant as the bifurcation is approached). The state $\overline{x}$ becomes less stable closer to the bifurcation and $J(\overline{x})$ gets less negative showing up in the indicator as an increase in variance.

Another popular early warning indicator is the time lagged autocorrelation

$$\alpha(t_{lag}) = e^{J(\overline{x})|t_{lag}|} \tag{15}$$

200 which measures the recovery time of the system to perturbations. Again, for the case where x is a real, scalar variable with first order dynamics subject to random (white noise) forcing $J(\overline{x})$ is a negative real number if the state is stable and $\alpha(t_{lag})$ is

just an exponentially decaying function of t_{lag}. As a bifurcation is approached $\mathcal{R}(J(\overline{x})) \rightarrow 0$ and the indicators $\sigma_x \rightarrow \infty$ and $\alpha(t_{lag}) \rightarrow 1$.

205 The temporal evolution of a scalar state variable x described by a linear first order (ODE) is constrained to only permit exponential decay from a perturbation. However, a real valued state variable x may have oscillatory behaviour and therefore must be described by higher order ODEs. In this case $\alpha(t_{lag})$ may have a more complicated functional form. For example, a system with second order dynamics can have an autocorrelation function with an oscillatory term. Relevant to our case, is the approach to a Hopf bifurcation whose $\alpha(t_{lag})$ has the generic form (Bury et al., 2020)

$$\alpha(t_{lag}) = e^{-\frac{|t_{lag}|}{\tau}} \cos(\omega t_{lag}) \tag{16}$$

210 For the Hopf bifurcation $J(x)$ is minimally a 2 by 2 real valued (non-symmetric) matrix with complex eigenvalues, λ and λ^*, that appear in conjugate pairs (the $*$ denotes complex conjugation). The real part of the complex eigenvalues of $J(x)$ ($\tau = -1/\mathcal{R}(\lambda)$) determines the exponential decay envelope of the autocorrelation function. This envelope decays over a longer timescale as the bifurcation is approached. Within this envelope there may also be oscillations with whose frequency is given by the imaginary part of $J(x)$, $\omega = \mathcal{I}(\lambda)$.

215 In most studies, the full autocorrelation function at all values of t_{lag} is generally not used - it is usually the value of the autocorrelation function at $t_{lag} = 1$ (the lag 1 autocorrelation) that is used. This often works well as it is more robust to sample size and signal to noise *provided* the oscillation period, $P = \frac{2\pi}{\omega}$, is large compared to the value of t_{lag} that is used to evaluate $\alpha(t_{lag})$ - formally, if $\omega t_{lag} \ll 1$, then equation 16 approximates to $\alpha(t_{lag}) \sim e^{-\frac{|t_{lag}|}{\tau}}$ i.e. it is a good indicator of the real part of the Jacobian eigenvalues and therefore of critical slowing down.

220 We will also use the autocovariance function, $R(t_{lag})$, which encodes information of both variance and autocorrelation i.e.

$$R(t_{lag}) = E[(x(t + t_{lag}) - \overline{x})(x(t) - \overline{x})] \tag{17}$$

or $R(t_{lag}) = \sigma_x^2 e^{J(\overline{x})|t_{lag}|}$. The variance is just given by $R(0)$ and $\alpha(t_{lag}) = \frac{R(t_{lag})}{R(0)}$.

4.1 Temporal EWS of the superrotation transition

We apply these early warning indicators to study the transition to superrotation as follows: We look at the statistics of the 225 fluctuations, $\delta u(t)$, around the mean zonal wind field state $\overline{u}$ where $\overline{u}$ is the time and area weighted spatial mean of a spherical segment centred on the equator with edges at $\theta_\pm = \pm 10^o$ latitude. An equatorial band centred on the equator is chosen to analyze the zonal wind field u because, as previously discussed, this is the most likely place to observe superrotation if it occurs. Formally, we compute $R(t_{lag})$ for $\delta u(t) = u(t) - \overline{u}$ where

$$u(t) = \frac{r}{A} \int\limits_{\phi=0}^{2\pi} d\phi \int\limits_{\theta=\theta_-}^{\theta_+} u(\theta, \phi, t) \cos\theta d\theta \tag{18}$$

230 ϕ is the longitude and $A = r \int_{\phi=0}^{2\pi} d\phi \int_{\theta=\theta_-}^{\theta_+} \cos\theta d\theta$ is the area of the spherical segment. We choose a section of the timeseries $u(t)$ starting at time t_s sufficiently long after the simulation spinup that the atmosphere is in an approximately stationary state.
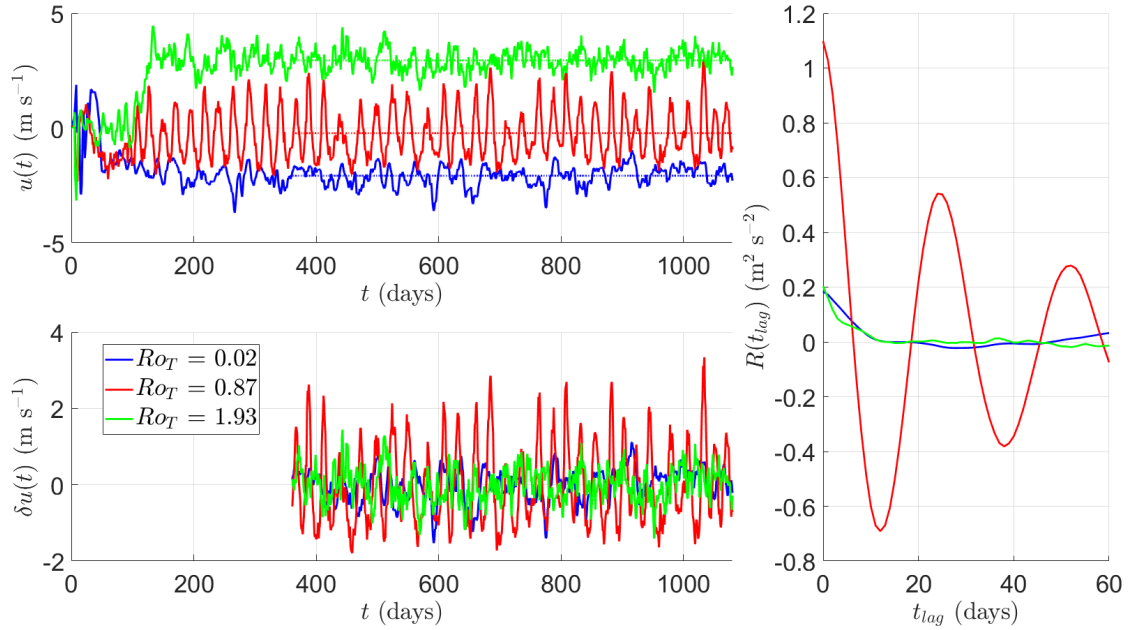
Figure 5. Mean u around an equatorial band: Upper LH panel - Mean zonal windspeed $u(t)$ in a spherical segment centred on the equator and with edges at $\pm 10^o$ latitude during a simulation of 3 years length (1080 days). Different colours correspond to a simulation with a different value of Ro_T. We have chosen to highlight $Ro_T \in \{0.02 \text{ (blue) } 0.87 \text{ (red) } 1.93 \text{ (green)}\}$. In the lower LH panel is $\delta u(t) = u(t) - \overline{u}$, the fluctuations in $u(t)$ around the temporal mean $\overline{u}$ over the last two years of the simulation as a function of Ro_T. Dotted lines indicate $\overline{u}$. RH panel: The autocovariance function $R(t_{lag})$ as a function of t_{lag}. This function is oscillatory for $RoT = 0.87$ (red line).

In the model configuration used, the atmosphere reaches a steady state after roughly 200 days although we use $t_s = 361$ days. The finish time t_f is chosen to be large for accurate determination of the statistical estimators. Ideally this would be $t_f \rightarrow \infty$ however due to computational time we limit to $t_f = 1080$ days. $u(t)$ is then averaged over a period $T = t_f - t_s$ to give

$$\overline{u} = \frac{1}{T} \int_{t_s}^{t_f} u(t)dt. \tag{19}$$

In the upper LH panel of figure 5, we plot $u(t)$ timeseries for selected values of Ro_T (0.02 is blue (Earth like), 0.87 is red (close to the transition) and 1.93 is green (fully superrotating)) over the 3 year simulation period. The mean u over the last two years ($\overline{u}$) is plotted as a corresponding colored dotted line. The lower LH plot shows the fluctuations around the mean, $\delta u(t)$, as a function of Ro_T. The larger, oscillatory response of $u(t)$ close to the transition is clearly visible in the timeseries. Either side of the transition (blue and green) the timeseries looks much more random and akin to first order noisy dynamics (such as an Ornstein-Uhlenbeck process).

In the RH panel of figure 5 we have plotted the autocovariance function (equation 17), $R(t_{lag})$, for each of the three selected Ro_T values during the last two years of each simulation. The value at $t_{lag} = 0$ is equivalent to the variance of u, σ_u^2. One can
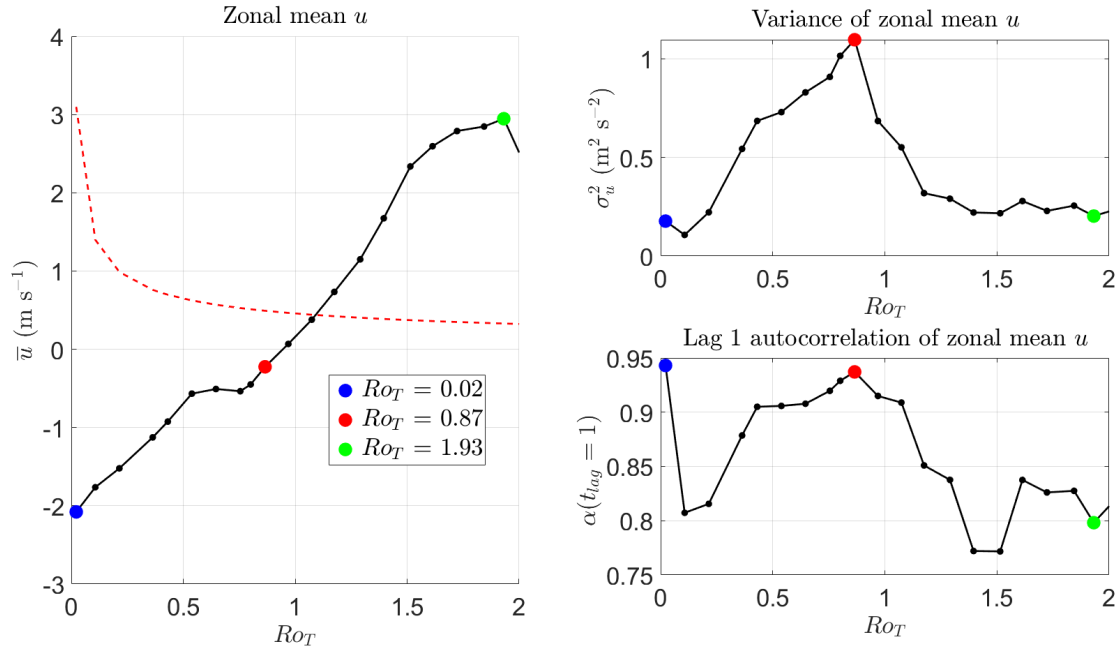
11

Figure 6. Usual early warning indicators: Each dot is an individual simulation. Coloured dots correspond to the same coloured simulations in figure 5. LH panel: Mean zonal windspeed $\overline{u}$ in a spherical segment centred on the equator with edges at $\pm 10^o$ latitude during the last 2 years of the simulation against RoT. The dotted red line is the threshold for superrotation to occur (u_{SR}). This is nonzero as the windspeed is averaged over a non-zero thickness latitude band. RH panels: Typical early warning indicators of a local bifurcation: upper RH panel, variance of mean zonal $u(t)$ and lower RH panel, lag 1 autocorrelation of mean zonal $u(t)$.

see close to the transition (red) that variance is much higher than either side of the transition (green and blue). One can also

245   see the functional form of $R(t_{lag})$ is also very different close to the transition showing an oscillation of around 25 days period contained in a exponential decay envelope ($e^{-\frac{|t_{lag}|}{\tau}}$) with an e-folding time of approximately $\tau \sim 35$ days (see equation 16). In contrast, either side of the transition, the response of $u(t)$ to perturbations is neither oscillatory or long lasting.

     In the LH panel of figure 6 we plot $\overline{u}$ in the equatorial spherical segment against Ro_T. Black dots are individual simulations, black lines connect these values. The dotted red line is the threshold $\overline{u}$ required for superrotation, u_{SR}, equation 4. This is

250   larger than the zero bound required for superrotation at the equator due to the finite latitude width of the spherical segment. Superrotation occurs approximately for $Ro_T > 1$. Interestingly, this plot is not monotonically increasing with Ro_T - there is a local maximum at $Ro_T \sim 0.54$ followed by a plateau to $Ro_T \sim 0.75$ below the superrotation threshold. There is another local (and global) maximum in $\overline{u}$ around $Ro_T \sim 1.9$ when the atmosphere is in a fully superrotating state. In the RH panels we plot the usual early warning indicators, variance of $u(t)$ (upper RH, σ_u^2) and lag 1 autocorrelation (lower RH, $\alpha(t_{lag} = 1$ day)).

255   Both indicators peak at $Ro_T = 0.87$, just below $\overline{u} \sim 0$ suggesting this is where the atmospheric state is least stable.
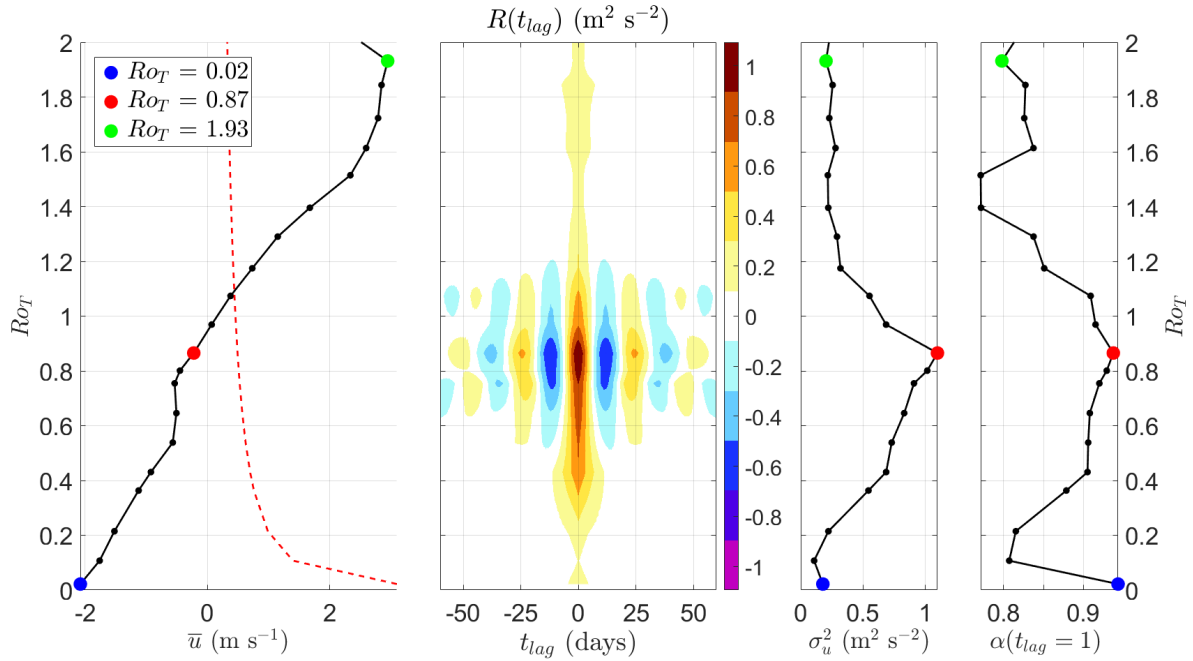
Figure 7. Early warning indicators: Similar to figure 6 with x and y axis variables swapped and with the full autocovariance function plotted ($R(t_{lag})$). Far LH panel: Mean zonal windspeed $\overline{u}$ vs RoT. Middle LH panel: Autocovariance function $R(t_{lag})$ and how it changes with RoT (y axis) and t_{lag}. Oscillations of 25 day period appear for values of $RoT \sim [0.5\ 1.2]$ and have a maximum in amplitude around $RoT \sim 0.9$. RH panels: For comparison with $R(t_{lag})$, typical early warning indicators (middle RH panel) variance of mean zonal $u(t)$ and (far RH panel) lag 1 autocorrelation of mean zonal $u(t)$.

As shown in the RH panel of figure 5, the autocorrelation function is not necessarily only exponentially decaying with increasing t_{lag} required for lag 1 autocorrelation to be a good indicator of the stability of the state. However as argued in section 4, it is a good indicator provided ωt_{lag} is much smaller than 1. In this case $\omega t_{lag} \sim 1/4$ so taking $\alpha(t_{lag} = 1\ \text{day})$ should be sufficient.

260   Motivated by the extra information in multiple t_{lag} values of the autocovariance function close to the superrotation transition, we plot $R(t_{lag})$ in the middle LH panel of figure 7 as it varies with RoT. As previously mentioned, $R(t_{lag})$ encodes both variance ($R(0)$) and lag 1 autocorrelation ($R(1)/R(0)$) as limiting cases making $R(t_{lag})$ a more complete information source and early warning precursor. We have plotted figure 6 with the axes flipped for ease of comparison to $R(t_{lag})$. $R(t_{lag})$ is an even function around t_{lag} with a maximal value at $R(0)$.

265   For values of $RoT < 0.57$ and $RoT > 1.2$, $R(t_{lag})$ is monotonically decreasing with $|t_{lag}|$ much like the exponential decay expected for first order dynamics. Oscillations in $R(t_{lag})$ start at $RoT \sim 0.57$ and remain until $RoT \sim 1.2$. The start of the oscillations coincides with the start of the plateau in $\overline{u}$. The end of the oscillatory phase coincides when the full spherical segment begins to superrotate ($\overline{u} > u_{SR}$ as shown by the red dotted line). Oscillations reach a maximum in amplitude at

$RoT \sim 0.87$ just before $\overline{u} \sim 0$. Throughout the range of their existence, the oscillations have a constant period of approximately

270   25 days.

5   Evidence of bistability

As previously mentioned, Suarez and Duffy (1992) found an abrupt transition to a superrotating state in a two layer GCM when the tropical heating was increased above a critical value. This tropical heating term was their control parameter and is different to the control parameter we alter in these experiments (the thermal Rossby number). Not only was the transition Suarez and

275   Duffy (1992) found abrupt, unlike the transition in this manuscript that seems smooth, the mean state also showed bistability i.e. two stable states exist for the same value of the control parameter. By slowly changing their control parameter across the transition's critical value from non-superrotating to a superrotating state and then slowly reversing the control parameter back again below the critical value, the superrotating state persisted to a new and lower critical value. This showed there was a bistable region in which stable superrotating and non-superrotating states can coexist.

280   We next investigate whether this type of bistability is present as our control parameter is slowly changed. This is done by slowly increasing the value of $RoT = 0.11$ through the transition at $RoT \sim 1$ and continuing up to $RoT = 1.64$. We will refer to this part of the simulation as the 'ramp up'. RoT is then slowly decreased from 1.64 back down to $RoT = 0.11$ at the same rate. We will refer to this part of the simulation as the 'ramp down'. As in the fixed RoT simulations, the magnitude of RoT is changed by altering the planetary radius r. Rather than a continuous change in RoT, we step RoT by a small increment of 0.11

285   every 2 years of simulation due to ease of implementation in the GCM. This gives a total simulation time of 58 years. Because of the step transition every 2 years, there is a small transient effect in the model state before settling back to a stationary state after approximately 200 days. To exclude any spurious effects in the early warning indicators, we calculate them only for the last year (360 days) of each step change in RoT.

In the upper LH panel of figure 8 we show how we vary RoT with time, solid black line indicating the ramp up of RoT

290   and the dotted black line indicating the ramp down of RoT. In the lower LH panel we plot $u(t)$ (grey line) in the equatorial band against time. The periods of increased variance are clearly visible between years 6 - 18 and 42 - 50 (also in the upper RH panel). Some of this large amplitude response is a short transient effect from adjustment to the step change in RoT although this quickly dies away. Black dots (ramp up) and black crosses (ramp down) in the lower LH panel are $\overline{u}$ in the last year of the step change so avoiding this transient effect. EWS variance and lag 1 autocorrelation are shown in the upper and lower RH

295   panels respectively.

Although $\overline{u}$ looks relatively symmetric about 30 years (the turn around point of the control parameter), the EWS do not. We plot these same quantities as a function of RoT in figure 9 to assess if there is any hysteresis when the control parameter is reversed and therefore whether bistability can be detected. In the LH panel we plot $\overline{u}$ on the ramp up (black dots) and ramp down (black crosses). Apart from a small region around the plateau in $\overline{u}$ between $RoT \sim 0.57 - 0.76$ there does not appear

300   to be any difference in the ramp up and ramp down values of $\overline{u}$. In the RH panels EWS differences are larger however this is probably due to the short length of the timeseries used to calculate these statistical estimators and small transient effects. Also,
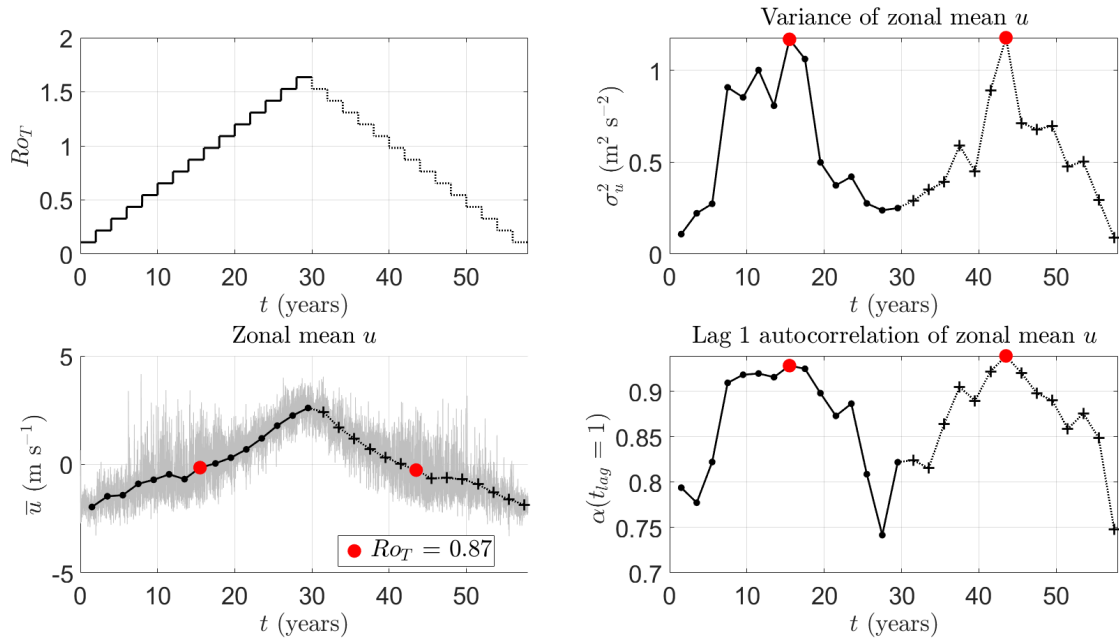
Figure 8. Ramped control parameter runs with time: Upper LH panel - Control parameter Ro_T value with simulation year. We start at $Ro_T = 0.11$ and make stepped increases of 0.11 every 2 years to mimic a slow continuous change in the control parameter as closely as possible. We ramp up Ro_T to 1.64 over a period of 30 years (black solid line) before slowly ramping down back to 0.11 over the next 28 years (dotted black line). Lower LH panel: Zonal mean wind speed $u(t)$ in the equatorial spherical segment with time (grey lines) and $\overline{u}$ (black dots - ramp up, black cross - ramp down) for the last year of each stepped change in Ro_T. Upper RH panel: Variance of $u(t)$ in the last year of each stepped change in Ro_T. Lower RH panel: Lag 1 autocorrelation $\alpha(t_{lag} = 1)$ of $u(t)$ in the last year of each stepped change in Ro_T.

as the standard error in the statistical estimators for a fixed sample size grows as autocorrelation increases, estimation should be worse in regions of large autocorrelation. Such a region exists for $Ro_T \in [0.4\ 1.2]$ and this is where we find the largest discrepancies. So we do not expect the small differences to be statistically significant.

305   Unlike Suarez and Duffy (1992) we find no evidence of bistability in the mean equatorial zonal wind speed. However, our control parameter is markedly different from theirs. This however does not completely rule out bistability - there may be smaller regions of Ro_T that these simulations have not been able to resolve.

6   Spatial precursors to the transition

The oscillations in the fluctuations, δu, around the mean zonal u in the equatorial band near the transition suggest the dynamics
310   must be second order or higher. Motivated by this and the interesting structure in the variance and autocovariance, we next use a method to diagnose any higher order dynamics of the fluctuations in the full global horizontal wind field $\delta \mathbf{v}(\theta, \phi, t) =$
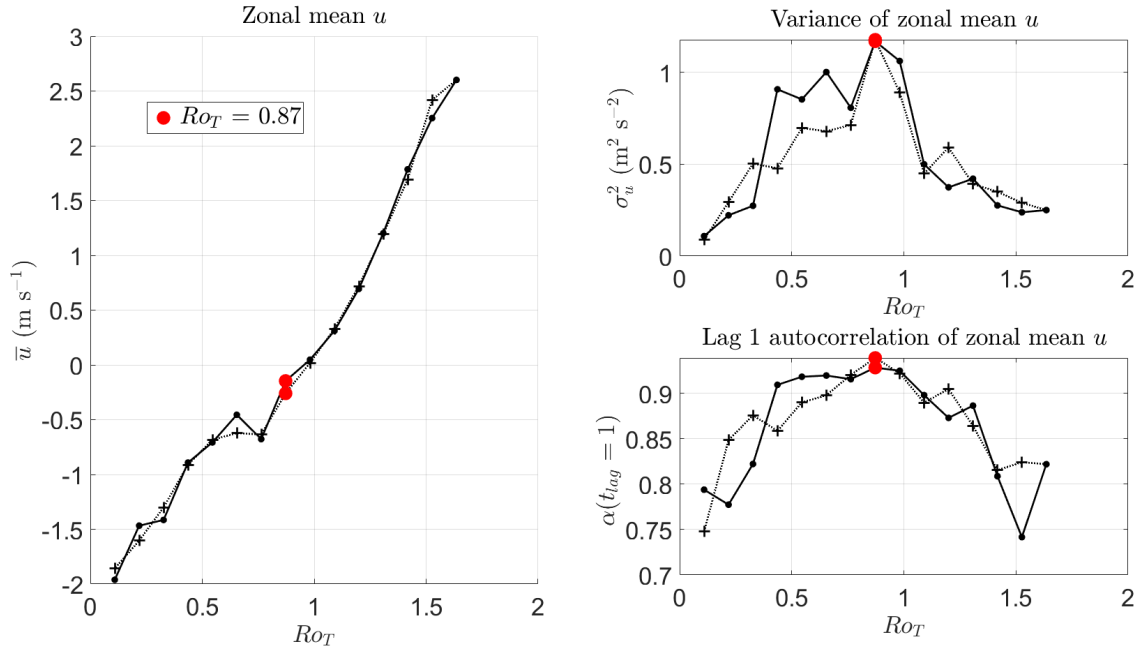
Figure 9. Ramped control parameter runs as a function of Ro_T, similar to figure 8 but with Ro_T as the x axis variable: LH panel - mean zonal wind speed $\overline{u}$ in the equatorial spherical segment for the last year of each stepped change in Ro_T. Black dots show values as Ro_T is on the ramped up path (years 0 - 30) and black crosses show those values as Ro_T is ramped back down (years 30 - 58). Upper RH panel: Variance of $u(t)$ in the last year of each stepped change in Ro_T. Lower RH panel: Lag 1 autocorrelation $\alpha(t_{lag} = 1)$ of $u(t)$ in the last year of each stepped change in Ro_T. Again black dots indicate values on the ramp up of Ro_T and black crosses on the ramp back down.

$(\delta u(\theta, \phi, t), \delta v(\theta, \phi, t))$. We look at the dominant spatial vector modes of $\delta \mathbf{v}$ and their stability. These modes are studied at the third vertical level $\sigma = (0.7 \ 0.79]$.

6.1 Vector valued state parameters

315   In section 4 the state parameter $x(t)$ was a real valued scalar and the theory developed to investigate the stability of a stationary state, $\overline{x}$, to small perturbations $\delta x(t)$, assumed first order dynamics. We remove the restriction to scalar x and therefore make higher order dynamics possible to describe and diagnose here. This is done by upgrading $\delta \mathbf{x}(t)$ to be an N component vector (vectors are denoted by bold type face). We can repeat the steps in section 4 for this generalization (see Williamson and Lenton (2015) for further details): We again want to study the response of small fluctuations $\delta \mathbf{x}(t)$ around some mean state $\overline{\mathbf{x}}$, to assess

320   the stability of that mean state - as the state becomes less stable approaching the transition, fluctuations become larger and longer lived. The state of the system in analogy to equation 9 is

$$\mathbf{x}(t) = \overline{\mathbf{x}} + \delta \mathbf{x}(t) \qquad (20)$$
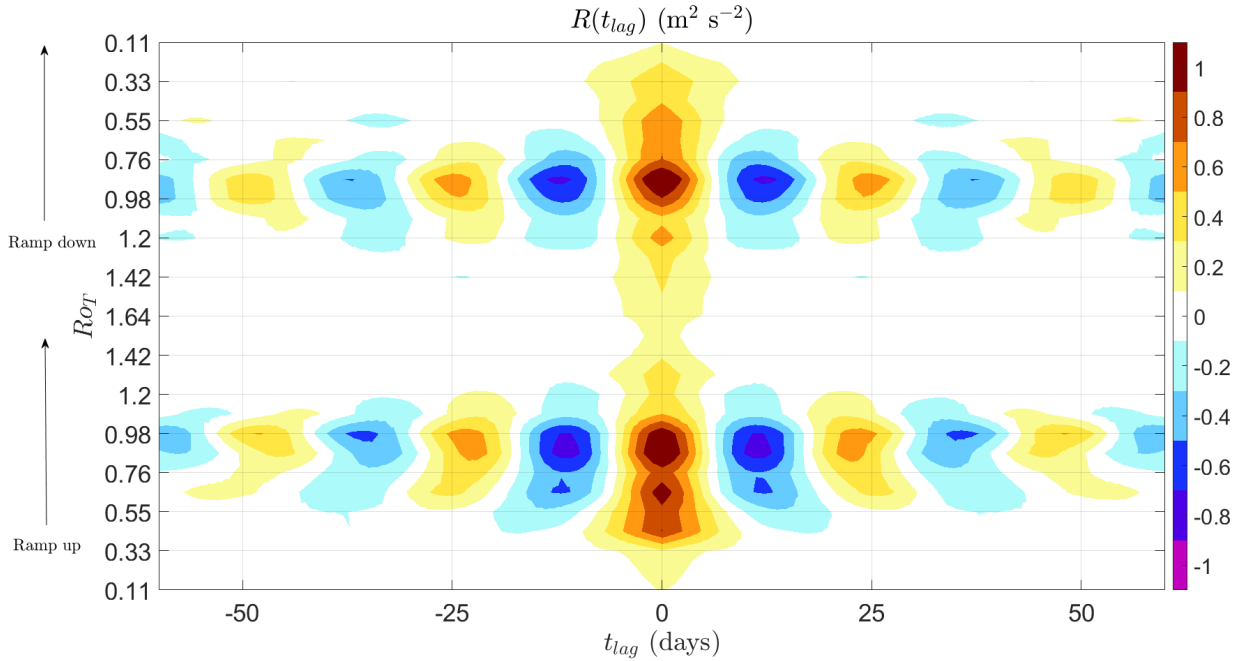
Figure 10. Ramped control parameter $R(t_{lag})$: Ramp up starts from the bottom of the y axis and ramp down from $Ro_T = 1.64$ continuing up the y axis. Although there are some small differences in ramp up and ramp down these are minor and oscillations appear in roughly the same place with the same amplitude and period.

The N components of the vector $\mathbf{x}(t)$ can be written explicitly as

$$\mathbf{x}(t) = (x_1(t), x_2(t), \ldots, x_{N-1}(t), x_N(t))^T \tag{21}$$

325　Similar expressions can be written for $\delta\mathbf{x}$ and $\overline{\mathbf{x}}$. The superscript T denotes the matrix transpose operator. The individual scalar components of $\mathbf{x}(t)$ are indexed with i which can take the values $i \in \{1, 2, \ldots, N-1, N\}$. Each of the x_i, is assumed to evolve autonomously, each according to a different, generally nonlinear function, $f_i(\mathbf{x})$. Note that each f_i has the multi-variable input $\mathbf{x}$. That is, f_i is a function of all $\{x_1, x_2, \ldots, x_N\}$ in general i.e. x_i are coupled, possibly nonlinearly. Formally, each x_i evolves according to $\dot{x}_i = f_i(\mathbf{x})$. Provided the fluctuations are not too large, the dynamics are approximated well by making a
330　multi-variable Taylor expansion of each $f_i(\mathbf{x})$ to first order around the mean state i.e. $f_i(\mathbf{x}) \approx f_i(\overline{\mathbf{x}}) + \sum_{j=1}^{N} J(\overline{\mathbf{x}})_{i,j}\delta x_j$ where instead of a single number describing the stability of the system, the Jacobian is now an $N \times N$ matrix encoding the linear couplings between the components of $\mathbf{x}$. The element in the ith row and jth column of J is given by $J(\overline{\mathbf{x}})_{i,j} = \frac{\partial f_i(\mathbf{x})}{\partial x_j}\big|_{\mathbf{x}=\overline{\mathbf{x}}}$. The dynamics of the fluctuations can be now be approximated with a linear first order ODE, however it is now a matrix equation

$$\dot{\delta\mathbf{x}} \approx J(\overline{\mathbf{x}})\delta\mathbf{x} \tag{22}$$

335　Analogous to the scalar x case, for a time invariant mean state $\overline{\mathbf{x}}$ (and time invariant $J(\mathbf{x})$), equation 22 has the solution

$$\delta\mathbf{x}(t) = e^{J(\overline{\mathbf{x}})t}\delta\mathbf{x}(0). \tag{23}$$

17

$J(\mathbf{x})$ still determines the behaviour and fate of small perturbations from $\overline{\mathbf{x}}$ and therefore $\overline{\mathbf{x}}$'s stability. However, $J(\mathbf{x})$ is a more complicated and general object than the single number of section 4 due to the couplings between the various δx_i (non-zero off-diagonal entries of J). One can uncouple the dynamics into N uncoupled modes, $\delta \tilde{x}_i$, by transforming each of the δx_i into a new basis (denoted by a tilde) that are a linear combination of the old δx_i i.e.

$$\delta \tilde{x}_i(t) = \sum_{j=1}^{N} a_j^{(i)} \delta x_j(t) \tag{24}$$

where $a_j^{(i)}$ are scalar (and possibly complex) coefficients. These new $\delta \tilde{x}_i$ are vectors although they behave like scalars and evolve independently of each other. Therefore one can treat the dynamics as N scalar (although generally complex, rather than real valued) first order ODEs such as the one in equation 10. The problem of finding this new uncoupled basis, where the off-diagonal entries of J are zero, is equivalent to finding the eigendecomposition of the Jacobian

$$J = Q \tilde{J} Q^{-1} \tag{25}$$

where $\tilde{J}$ is a diagonal matrix (only non-zero entries are on the diagonal) with N eigenvalues, each labelled by λ_i on the diagonal of $\tilde{J}$ associated to the N eigenvectors of J, denoted q_j, given by the jth column of matrix Q. The same Q also diagonalizes the matrix $e^{J(\overline{\mathbf{x}})t}$. So the new basis in equation 24 is simply given by $\delta \tilde{x}_i = \sum_{j=1}^{N} (Q^{-1})_{i,j} \delta x_j$ where $(Q^{-1})_{i,j} \equiv a_j^{(i)}$ give the coefficients to uncouple the equations. This new basis $\delta \tilde{x}_i$ go by several names i.e. they are often known as linear, critical, normal or the eigenmodes modes.

How each of the $\delta \tilde{x}_i$ evolve now reduces to the N equations

$$\delta \tilde{x}_i(t) = e^{\lambda_i t} \delta \tilde{x}_i(0). \tag{26}$$

and therefore again there are three possible fates of an initial perturbation of amplitude $\delta \tilde{x}_i(0)$ on mode i depending on the sign of the real part of each of the λ_i: (i) The real part of λ_i is negative ($\mathcal{R}(\lambda_i) < 0$); the initial fluctuation in the critical mode $\delta \tilde{x}_i(0)$ decays and this particular mode will be stable to perturbations. In this case a recovery time for this mode can be defined as $\tau_i = -1/\mathcal{R}(\lambda_i)$. (ii) The real part of λ_i is positive ($\mathcal{R}(\lambda_i) > 0$); any initial fluctuation on this mode will get exponentially larger with time and the mode will be unstable. (iii) The real part of λ_i is zero i.e. $\mathcal{R}(\lambda_i) \to 0$. In this case, perturbations will not grow or decay in this mode. This neutral stability occurs at a bifurcation.

The evolution of the fluctuations around the mean of the entire system is described by a linear superposition of all N modes i.e.

$$\delta \mathbf{x}(t) = \sum_{i=1}^{N} e^{\lambda_i t} \delta \tilde{x}_i(0) \tag{27}$$

therefore all N modes must be stable for the overall system to be stable. If one or more of the modes are unstable, as time increases the unstable mode with the most positive real part will swamp the response of the other $N-1$ modes and cause the entire system to be unstable. That is, for a stable system, the requirement must be $\mathcal{R}(\lambda_i) \leq 0 \; \forall i$. Provided all the modes are stable, the $\delta \tilde{x}_i$ with the least negative $\mathcal{R}(\lambda_i)$ will dominate the dynamics of the system simply because they decay more slowly

(larger τ_i) than those modes associated to shorter τ_i (more negative $\mathcal{R}(\lambda_i)$). That is, the dynamics of the entire system may be well described by just a few (n) modes, where $n < N$, with the largest timescales such that

$$\delta\mathbf{x}(t) \approx \sum_{i=1}^{n} e^{\lambda_i t}\delta\tilde{x}_i(0) \tag{28}$$

370 where λ_i are ordered in increasing size i.e. $\mathcal{R}(\lambda_i) \geq \mathcal{R}(\lambda_{i+1})$. An extreme example is when a local bifurcation is approached and the timescale of one (or more) of the modes $\tau_i \to \infty$ ($\mathcal{R}(\lambda_i) \to 0$) and dominates the dynamics to such a degree the system can be described by just that one (or more) mode.

The eigenvalues λ_i can also have imaginary components. These give rise to oscillations in the associated mode with angular frequency $\omega_i = \mathcal{I}(\lambda_i)$. For a real valued J, complex λ_i always occur in complex conjugate pairs with associated complex

375 conjugate eigenvectors. If eigenvalues (and therefore eigenvectors) are complex, the superposition with it's conjugate mode gives a real, but time evolving spatial mode. Explicitly for a single, dominant complex (oscillatory) mode ($\mathcal{R}(\lambda_1) \gg \mathcal{R}(\lambda_i)$, $\forall i \neq 1$), the dynamics is

$$\delta\mathbf{x}(t) \sim e^{\lambda_1 t}\delta\tilde{x}_1 + e^{\lambda_1^* t}\delta\tilde{x}_1^* \tag{29}$$

$$\sim e^{-\frac{t}{\tau_1}}\left[\cos(\omega_1 t)\mathcal{R}(\delta\tilde{x}_1) - \sin(\omega_1 t)\mathcal{I}(\delta\tilde{x}_1)\right] \tag{30}$$

380
$$\sim e^{-\frac{t}{\tau_1}}\cos(\omega_1 t + \phi_1)|\delta\tilde{x}_1| \tag{31}$$

That is the mode spatially oscillates between its real and imaginary parts at angular frequency ω_1. In the last line we have defined a vector phase $\phi_1 = \arg(\delta\tilde{x}_1)$.

For a dominant real mode, the dynamics is

$$\delta\mathbf{x}(t) \sim e^{\lambda_1 t}\delta\tilde{x}_1 \tag{32}$$

385
$$\sim e^{-\frac{t}{\tau_1}}\delta\tilde{x}_1 \tag{33}$$

since $\omega_1 = 0$ and $\mathcal{I}(\delta\tilde{x}_1) = 0$, there is no conjugate mode. A mode associated to a real eigenvalue has real eigenmode and therefore the spatial pattern remains fixed, decaying exponentially and uniformly from the constant multiplier on the pattern $e^{-\frac{t}{\tau_1}}$. This case is analogous to the first order dynamics scalar case of section 4; the constant multiplier being the lag 1 autocorrelation and the spatial mode being analogous to the scalar variable x.

390 One may wonder how equation 22 describes higher order dynamics since it is a first order ODE. A Nth order system can be written as a first order vector ODE with N dimensions. For example, the third order system

$$\dddot{x} + a\ddot{x} + b\dot{x} + cx = 0 \tag{34}$$

can be written as a first order vector ODE in 3 dimensions by making the identifications $y = \dot{x}$ and $z = \dot{y}$ so that equation 34 can be written

395 $$\dot{x} = y \tag{35}$$

$$\dot{y} = z \tag{36}$$

$$\dot{z} = -cx - by - az \tag{37}$$

or as a first order vector ODE

$$\begin{pmatrix} \dot{x} \\ \dot{y} \\ \dot{z} \end{pmatrix} = \begin{pmatrix} 0 & 1 & 0 \\ 0 & 0 & 1 \\ -c & -b & -a \end{pmatrix} \begin{pmatrix} x \\ y \\ z \end{pmatrix} \tag{38}$$

400   which can be written more compactly in the same form as equation 22

$$\dot{\mathbf{x}} = J\mathbf{x}. \tag{39}$$

Under the assumption of white noise forcing (or equivalently independent errors on δx_i) one can reconstruct J from time-series of the δx_i, each timeseries sampled at an interval Δt between time steps as follows (see Williamson and Lenton (2015) for details)

405   $$e^{J(\mathbf{x})\Delta t} = A\Sigma^{-1} \tag{40}$$

Where Σ is the covariance matrix of $\delta \mathbf{x}$ and A is the lagged covariance matrix i.e.

$$\Sigma = E[\delta\mathbf{x}_t \delta\mathbf{x}_t^T] \tag{41}$$

$$A = E[\delta\mathbf{x}_{t+\Delta t} \delta\mathbf{x}_t^T] \tag{42}$$

One can then find the eigenmodes and eigenvalues of J (and hence their stability). For vector valued $\mathbf{x}$, the analogous EWS to

410   the scalar case (section 4) are now matrix valued i.e.

$$A\Sigma^{-1} \equiv \alpha(t_{lag}) \tag{43}$$

$$\Sigma \equiv \sigma_x^2 \tag{44}$$

however we now have N modes (eigenvectors of J) associated to N timescales (eigenvalues of J). Early warning signals autocorrelation and variance are still functions of $J(x)$ but they are also now also matrices (autocovariance and covariance

415   matrices respectively). This technique is also known as Principle Oscillation Pattern (POP) analysis (Hasselmann, 1988). We will analyze the properties of J in the following as this is what ultimately determines stability (and the EWS which are functions of J).

6.2   Spatial EWS of the superrotation transition

We now apply the vector technique described in the last subsection to the full spatial horizontal vector wind field $\delta\mathbf{v}(\theta, \phi, t)$

420   and diagnose the dominant eigenvalues and eigenmodes as Ro_T is varied through the superrotation transition.

We identify the vector $\delta \mathbf{x}(t)$ at each time t in equation 20 to have components $\delta x_i(t)$ that are the $\delta u(\theta_i, \phi_i, t)$ at each horizontal grid box labelled i in the GCM with coordinates (θ_i, ϕ_i) at vertical level $\sigma = 0.7$. This two dimensional horizontal field is area weighted by grid box size, reshaped into a column vector and concatenated with the analogous field of $\delta v(\theta_i, \phi_i, t)$. Time is also a discrete variable in the GCM output having integer day values with interval $\Delta t = 1$ day. We label the full vector

425    $\delta \mathbf{v}_t$.

As the full resolution horizontal field in this configuration of Isca has $64 \times 128 = 8192$ grid boxes for each field of u and v, the vector has 16 384 components. The resulting reconstructed J would therefore be a real valued, although non-symmetric 16384×16384 matrix whose calculation would be computationally costly. To reduce this cost, we project fields of δu and δv at each time t on to their n largest empirical orthogonal functions (EOFs), the dominant eigenvectors of the covariance matrix Σ,

430   to capture the dominant dynamics of $\delta \mathbf{v}(t)$ (see von Storch and Zwiers (1999) for a description of the EOF technique). We use $n = 60$ which captures between 76% and 88% of the total variance depending on the value of Ro_T. We have experimented with using larger n and while more of the total variance is captured, the results presented below remain invariant. This is because we are interested in the dominant modes of the dynamics (largest eigenmodes of J) and these are well captured by the projections on to the leading EOFs.

435   Using the reduced EOF basis for $\delta \mathbf{v}_t$ we calculate A and Σ using the last two years of each Ro_T simulation and therefore infer J using equations 40 and 41 for the full global horizontal vector windfield fluctuations. Performing an eigendecomposition to find the dominant modes and their stabilities on each reconstructed J results in figure 11.

6.2.1 Eigenvalues of J: Timescales and oscillation frequencies

The spectrum of each J (the first 20 eigenvalues, λ_i $i \in \{1, 2, \cdots, 20\}$, where $\mathcal{R}(\lambda_i) \geq \mathcal{R}(\lambda_{i+1})$) as a function of Ro_T are

440   shown in the middle two panels of figure 11. Generally each λ_i has a real and imaginary part. The real part $\mathcal{R}(\lambda_i)$ determines how dominant the associated eigenmode is in the dynamics with less negative values being more dominant. Equivalently, the eigenmodes with the largest e folding timescales, τ_i, dominate the dynamics (recall $\tau_i = -1/\mathcal{R}(\lambda_i)$). We choose to represent the real part of each eigenvalue as a timescale τ_i in the upper middle plot.

The imaginary part of each eigenvalue $\omega_i = \mathcal{I}(\lambda_i)$ determines the oscillation frequency of the associated eigenmode. We

445   choose to represent the imaginary part of each eigenvalue as the period of the oscillation $P = \frac{2\pi}{\omega_i}$ in the lower middle plot.

Each black dot represents one of the 20 leading eigenvalues. At low values of Ro_T, the timescales of the leading modes are very close or the same (degenerate) within calculated error bounds from finite sample length $t_f - t_s$. This effective degeneracy in J can result in some non-uniqueness in the decomposed eigenmodes. In contrast, leading τ_i become well separated for $Ro_T > 0.4$ and eigenmodes can be reliably inferred. We have highlighted how the τ_i of three leading eigenmodes around the

450   transition change with Ro_T in the upper middle panel and the associated oscillation periods P in the lower middle panel. These are colour coded to the associated spatial mode i.e. black is the Earth-like mode (upper LH panel), red is the 'precursor' mode (lower LH panel), blue is the 'superrotation' mode (upper RH panel) and magenta is the 'swirly' mode (lower RH panel).
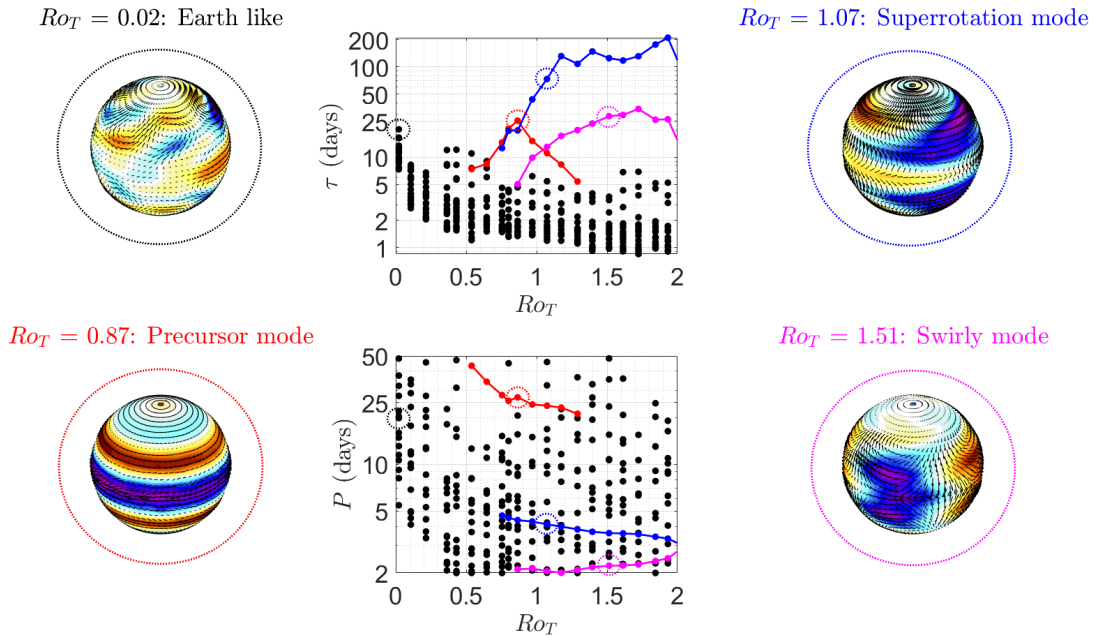
Figure 11. Spatial precursors of the superrotation transition: The 20 leading eigenvalues of the Jacobian of the global horizontal wind field fluctuations, $\delta\mathbf{v}(t)$, around the mean state $\overline{\mathbf{v}}$ as Ro_T changes. The real part of the eigenvalues, determining the stability and the dominance in the dynamics of the associated mode, are shown in the middle upper panel as a timescale $\tau = -1/\mathcal{R}(\lambda_i)$. The corresponding imaginary part of the eigenvalues, determining the oscillation frequency of the associated mode, is shown as an oscillation period ($P = \frac{2\pi}{\mathcal{I}(\lambda_i)}$). Three of the largest eigenmodes are colour coded and tracked through different values of Ro_T to show how they evolve in the spectrum of J (middle panels). In the end columns of the figure are the eigenmodes associated to the color coded eigenvalues. The exact Ro_T value of each snapshot of the mode in the eigenvalue plots is denoted by a dotted circle around each eigenvalue. Eigenmodes are dynamic but are shown at $t = 0$ before they oscillate with period P and damping takes place (exponential decay with timescale τ). The colour coding indicates $\delta u(\theta, \phi, t)$ with $\delta u < 0$ (blue) and $\delta u > 0$ (red) shown. Arrows show the full vector field $\delta\mathbf{v}(\theta, \phi, t)$. The modes are Earth-like (upper LH, black), precursor (lower LH, red), superrotation (upper RH, blue) and swirly (lower RH, magenta).

6.2.2 Eigenvectors of J: Spatial mode structure

The leading modes of J, the eigenvectors associated to the eigenvalues with the largest τ_i, around the transition to a superrotat-
455 ing state are discussed next. These are dynamic modes that change with time according to equation 29. We have tried to show their evolution through one full oscillation in figure 12. (Animations of these modes are also available, see video supplement at the end of the manuscript.) These modes show how the vector wind field adjusts when perturbed from its mean state. A analogy would be the most visible pattern of a drum skin vibration (the dominant eigenmode) from rest (the mean state) when hit with a drum stick (the perturbation).

460   **Earth-like mode (black, upper LH panel, fig 11)**: This spatial pattern can only be identified for $Ro_T = 0.02$ which is an Earth-like simulation. Although it is the dominant mode, due to the close spacing of the τ_i at $Ro_T = 0.02$, this pattern alone does not account for very much of the dynamics of $\delta\mathbf{v}$. It has a time scale of $\tau \sim 20$ days and an oscillation frequency of $P \sim 20$ days. This mode is very jet stream like, capturing the mid-latitude instabilities. The evolution of this mode through one full cycle is shown in the top row of figure 12.

465   **Precursor mode (red, lower LH panel, fig 11)**: The red mode spatial pattern appears at $Ro_T \sim 0.5$ and is the dominant mode in the fluctuation dynamics between $Ro_T \approx 0.75$ and $Ro_T = 0.87$ although a second mode, the 'superrotation' mode is similar in size during this Ro_T interval. At $Ro_T = 0.87$ the mode peaks in τ with a decay timescale of $\tau \sim 25$ days and this is when the early warning indicators of section 4 all peak just before the transition. It is responsible for the shape of the variance of zonal mean u in figure 6. It is also responsible for the oscillating autocovariance function $R(t_{lag})$ in figure 7 as it is

470 a zonal wavenumber zero mode with $P \sim 25$ days. This is why we refer to this mode as the 'precursor mode'. After the peak, this mode then reduces quickly in importance until it is no longer detectable at $Ro_T \sim 1.3$. It is the third largest mode from $Ro_T > 1$. The evolution of this mode through one full cycle is shown in the second row of figure 12.

    Superrotation mode (blue, upper RH panel, fig 11): The blue mode alone clearly dominates the dynamics (largest τ_i) when the atmosphere becomes fully superrotating for $Ro_T \geq 1$. It is also an important component of the fluctuation dynamics

475 around the transition at $Ro_T \sim 0.75$ when it is a similar size to the red 'precursor' mode. This is also when it first appears as a mode of J. We call this mode the 'superrotation' mode. The e folding timescale of this mode gets as large as $\tau \sim 200$ days past $Ro_T > 1$ and has an oscillation frequency of $P \sim 4$ days. It is a mode with a zonal wavenumber of one. The evolution of this mode through one full cycle is shown in the third row of figure 12. This is similar to the one identified by Mitchell and Vallis (2010) for a fully superrotating state ($Ro_T = 10.5$) in the context of zonal mean zonal wind interactions.

480   **Swirly mode (magenta, lower RH panel, fig 11))**: The magenta mode is significant in the fluctuation dynamics after the superrotation transition, particularly for larger values of Ro_T although it is never the dominant mode. It is a mode with zonal wavenumber 2 and oscillation frequency $P \sim 2$ days. We call this mode, the 'swirly' mode. The evolution of this mode through one full cycle is shown in the bottom row of figure 12.

    The start of the plateau in $\overline{u}$ in figure 6 coincides with the appearance of the 'precursor' mode and the end with the appearance

485 of the 'superrotation mode'. One could argue the plateau in $\overline{u}$, is also a precursor to the superrotation transition. However, it is the appearance of the precursor mode and its properties that produce the EWS (rising variance, increasing $\alpha(t_{lag})$, $R(t_{lag})$) and herald the transition to superrotation.

7   Discussion & Conclusion

The motivation for this study came from Isaac Held's excellent blog (Held, 2016). One of the posts on that blog introduced

490 the work of Suarez and Duffy (1992) who observed an abrupt transition to a superrotating state in a idealised two vertical level GCM as a longitude dependent heat source in the tropics was increased. The atmospheric state in this model also showed bistability i.e. both superrotating and regular, present day atmospheric states were stable for the same value of tropical heating.
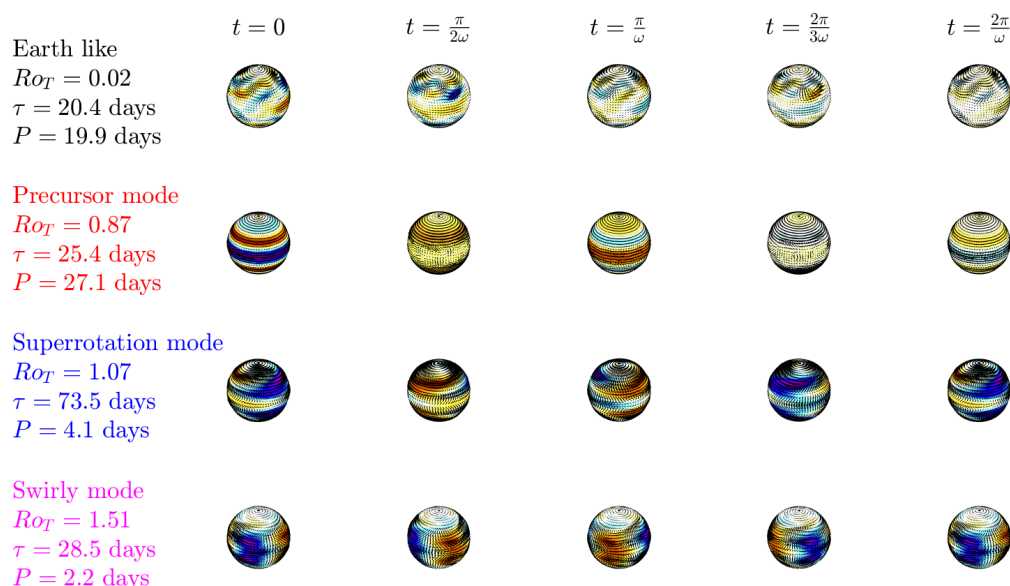
Figure 12. Dynamic evolution of the eigenmodes of J: As the eigenmodes of $\delta\mathbf{v}(\theta,\phi,t)$ change with time according to equation 29 we have tried to show this evolution through one full oscillation (a movie is available online) of the four selected modes in figure 11. The colour coding indicates $\delta u(\theta,\phi,t)$ with $\delta u < 0$ (blue) and $\delta u > 0$ (red) shown. Arrows show the full vector field $\delta\mathbf{v}(\theta,\phi,t)$. The columns show the mode at the start of the cycle ($t = 0$) and advance by $1/4$ of a cycle left to right. Exponential decay from τ is also shown as the color coding becoming more washed out as t advances. The rows of the figure show the modes: Earth-like (upper row, black), precursor (second row, red), superrotation (third row, blue) and swirly (bottom row, magenta).

This example has many similarities with other climate tipping points (Lenton et al., 2019) - abrupt changes in state caused by relatively small changes in forcing parameters. These are generally regarded as low probability, high risk events. One such example is the Atlantic meridional overturning circulation (AMOC) that can abruptly change from an 'on' to 'off' state as freshwater flux into the North Atlantic is increased (Stommel, 1961; Vellinga and Wood, 2002; Mecking et al., 2016). The AMOC can also show bistability; the off state can persist as the freshwater flux is decreased back below the original threshold. There are a variety of other widely studied climate tipping points - the Amazon rainforest, Greenland ice sheet and Arctic sea ice to name a few - however superrotation has not received the same attention. One of the motivations of this work was to begin to correct this deficiency.

Unlike Suarez and Duffy (1992), where the control parameter varied (the tropical heating) is arguably relevant to future anthropogenic climate change, our control parameter, the thermal Rossby number (Ro_T), a non-dimensional number that controls the global atmospheric dynamics, is probably not relevant to future climate change. And unlike the abrupt transition in equatorial mean zonal $\overline{u}$ observed in Suarez and Duffy (1992), our transition is smooth as the control parameter is varied.

505 The third difference is that we have not been able to detect bistability (section 5). Nevertheless, the simulations reported here do show early warnings of the transition and serve as a test bed for the second motivation of this manuscript, namely whether we can detect this transition before it happens.

The usual early warnings of local bifurcation type tipping (rising variance and autocorrelation, section 4) all increase before the superrotation transition, simultaneously peaking at $Ro_T = 0.87$ when calculated for the equatorial zonal wind speed u.

510 These peaks show that fluctuations around the mean state wind field grow in magnitude and persist for longer close to the superrotation transition, indicative of critical slowing down near a local bifurcation.

In addition, the full autocovariance function, $R(t_{lag})$, showed oscillations of period $P \sim 25$ days that became increasingly less damped as the transition was approached, reminiscent of a Hopf type bifurcation (see equation 16). In a Hopf bifurcation, a pair of complex conjugate eigenvalues of the Jacobian move in the complex plane from the negative real half and cross the

515 imaginary axis at the point of bifurcation (see Strogatz (2001) for details). Before the bifurcation, this results in critical slowing down in the dynamics (increasingly less negative $\mathcal{R}(\lambda)$) as well as oscillations of frequency $\omega = \mathcal{I}(\lambda)$. These are observed in the superrotation transition.

The presence of oscillations in δu motivated us to use a more general technique to study the transition. The usual theory of EWS relies on scalar state variables and first order dynamics. This does not permit oscillations or higher order dynamics. We

520 gave a pedagogical introduction to the more general theory in section 6 and calculated the Jacobian and normal modes for the full global vector wind field $\delta \mathbf{v}(\theta, \phi)$. EWS are designed to detect changes in the stability of the mean state and therefore must be functions of the Jacobian's eigenvalues which entirely describe the linear stability of the mean state. We therefore chose to study the eigenvalues and eigenmodes of the Jacobian as they are the sole determinant of traditional EWS based on linear stability analysis.

525 When a system approaches an abrupt transition resulting from a local bifurcation, often a single eigenmode of the Jacobian starts to dominate the dynamics. Close to the transition we found two eigenmodes (or spatial patterns) that the fluctuations, $\delta \mathbf{v}$, preferentially oscillate in, before slowly decaying back towards the mean state $\overline{\mathbf{v}}$. One of these modes, the precursor mode, was a zonal wavenumber zero mode that we attribute to the 25 day oscillations in the equatorial zonal mean δu as well as the rise in variance and autocorrelation seen in section 4. There is also a second mode of roughly the same size around the transition

530 - the superrotation mode - a zonal wavenumber one mode that comes to dominate the dynamics as the atmosphere becomes fully superrotating. Detecting the precursor mode in the spatial or temporal correlations would serve as the best EWS. These modes were calculated for the global windfield. It is plausible that the precursor mode would be even more significant in the dynamics of the tropics if the spatial analysis was performed over just the tropical region, rather than the entire globe.

One may wonder why oscillations are not observed for $Ro_T > 1.3$ after the precursor mode disappears from the dynamics

535 in the scalar EWS even though the dominant modes in this regime, the superrotation mode and the swirly mode, are oscillatory with periods $P \sim 4$ and $P \sim 2$ days respectively. This is due to their zonal wavenumbers - remember equatorial zonal u was averaged over a latitude band in section 4. For nonzero zonal wavenumbers, the average will be always be zero as there are an equal numbers of peaks and troughs. A zonal wavenumber zero pattern like the precursor mode however, will have a non-zero average in a zonal mean.

540   There remain questions about the dynamical mechanisms giving rise to the observed eigenmodes around the transition. There is a detailed analysis in Mitchell and Vallis (2010). Outstanding questions in this domain are left to a future study.

The degree of spatial correlation in the fluctuations, particularly in the precursor mode, is reminiscent of a phase transition (Anderson, 1984). Traditionally, phase transitions are studied via the statistics of the spatial fluctuations around the mean state. The hallmarks of a phase transition are diverging correlation length and correlation time (resulting in critical slowing down) as

545   well as an abrupt change in the order parameter of the state. In particular, continuous phase transitions have spatial correlation functions that are described by a power law at the critical point giving rise to scale invariant physics and often involve a broken symmetry. What are the similarities with the transition to superrotation? Diverging correlation time is present (τ) and diverging correlation length is qualitatively present (as seen in the pattern of the precursor mode, at least zonally) although we have not formally calculated spatial correlation functions. Dylewsky however has found quantitative evidence via a neural

550   network trained on the spatial information from a 2D Ising model phase transition - this trained neural network does predict the superrotation transition clearly before it occurs (Dylewski, pers. comm., see also Dylewsky et al. (2023)).

Detection of a power law at the transition would also require long simulations very close to, or at the critical point of Ro_T. Long simulations are needed at the transition because of the diverging correlation time (a.k.a. critical slowing down). There are also broken symmetries present: The Jacobian's eigenvalues look to be very similar in value (degenerate), at least to the error

555   in their estimation, making the dynamics of the fluctuations invariant under high dimensional symmetry groups - technically continuous orthogonal groups (spatial rotations of the eigenmodes in their vector basis representation) of the same dimension as the degree of the degeneracy of J. These spatial symmetries are broken to lower dimensional discrete symmetry groups close to the transition when the eigenvalues of J become more widely separated and a few eigenmodes dominate the dynamics of the fluctuations.

560   The Landau theory of phase transitions (Landau, 1937) starts with identifying a suitable order parameter, and then expanding the free energy as a power series of the order parameter. The order parameter takes the value zero in a disordered phase and a non-zero value when the system is 'ordered'. It is not clear what the order parameter would be for our case however it is not always obvious in many instances. For example, in a Bose-Einstein condensate, it is related to the off-diagonal long range order of the one particle density matrix and in the gas-liquid transition it is the density difference between gas and liquid. It would

565   be interesting to look for power laws in the spatial correlation function and determine the critical exponents, the exponents that determine the universality class of the transition should they exist.

Although the probability of transitioning to a equatorial superrotating atmospheric state under future climate change seems unlikely, it is not zero (see Held (2016)). There is (limited) evidence that it has happened in the past and can happen in the future (Huang et al., 2001; Caballero and Huber, 2010; Tziperman and Farrell, 2009). As with other tipping points, this makes

570   superrotation a low probability but high risk event. It would be interesting to repeat the experiment of Suarez and Duffy (1992) with the Isca framework, namely a more relevant way of transitioning to superrotation under climate change, and see if the EWS identified here are still present.

Code and data availability. Data and code is available from the corresponding author.

Video supplement. Animations of the leading eigenmode evolution (figure 12) are available here ...

580 **References**

Anderson, W.: Basic Notions Of Condensed Matter Physics, Basic Books, https://books.google.co.uk/books?id=-QRBAQAAIAAJ, 1984.

Armstrong McKay, D. I., Staal, A., Abrams, J. F., Winkelmann, R., Sakschewski, B., Loriani, S., Fetzer, I., Cornell, S. E., Rockström, J., and Lenton, T. M.: Exceeding 1.5°C global warming could trigger multiple climate tipping points, Science, 377, eabn7950, https://doi.org/10.1126/science.abn7950, 2022.

585 Arnold, N. P., Tziperman, E., and Farrell, B.: Abrupt Transition to Strong Superrotation Driven by Equatorial Wave Resonance in an Idealized GCM, Journal of the Atmospheric Sciences, 69, 626–640, https://doi.org/https://doi.org/10.1175/JAS-D-11-0136.1, 2012.

Ashwin, P., Wieczorek, S., Vitolo, R., and Cox, P.: Tipping points in open systems: Bifurcation, noise-induced and rate-dependent examples in the climate system, Philos. T. Roy. Soc. A, 370, 1166–1184, 2012.

Bury, T. M., Bauch, C. T., and Anand, M.: Detecting and distinguishing tipping points using spectral early warning signals, Journal of The
590 Royal Society Interface, 17, 20200 482, https://doi.org/10.1098/rsif.2020.0482, 2020.

Caballero, R. and Carlson, H.: Surface Superrotation, Journal of the Atmospheric Sciences, 75, 3671–3689, https://doi.org/10.1175/JAS-D-18-0076.1, 2018.

Caballero, R. and Huber, M.: Spontaneous transition to superrotation in warm climates simulated by CAM3, Geophysical Research Letters, 37, https://doi.org/10.1029/2010GL043468, 2010.

595 Dakos, V., Scheffer, M., van Nes, E. H., Brovkin, V., Petoukhov, V., and Held, H.: Slowing down as an early warning signal for abrupt climate change, P. Natl. Acad. Sci. USA, 105, 14 308–14 312, 2008.

Ditlevsen, P. D. and Johnsen, S. J.: Tipping points: Early warnings and wishful thinking, Geophys. Res. Lett., 37, L19 703, 2010.

Dylewsky, D., Lenton, T. M., Scheffer, M., Bury, T. M., Fletcher, C. G., Anand, M., and Bauch, C. T.: Universal early warning signals of phase transitions in climate systems, Journal of The Royal Society Interface, 20, 20220 562, https://doi.org/10.1098/rsif.2022.0562, 2023.

600 Gordon, C. T. and Stern, W. F.: A Description of the GFDL Global Spectral Model, Monthly Weather Review, 110, 625–644, https://doi.org/https://doi.org/10.1175/1520-0493(1982)110<0625:ADOTGG>2.0.CO;2, 1982.

Hasselmann, K.: PIPs and POPs: The reduction of complex dynamical systems using principal interaction and oscillation patterns, Journal of Geophysical Research: Atmospheres, 93, 11 015–11 021, https://doi.org/https://doi.org/10.1029/JD093iD09p11015, 1988.

Held, H. and Kleinen, T.: Detection of climate system bifurcations by degenerate fingerprinting, Geophys. Res. Lett., 31, L23 207, 2004.

605 Held, I. M.: Equatorial superrotation in Earth-like atmospheric models, 1999.

Held, I. M.: Superrotation, idealized models, and GCMs, https://www.gfdl.noaa.gov/blog_held/68-superrotation-idealized-models-and-gcms/#more-36652 [Accessed: (27th July 2023)], 2016.

Held, I. M. and Suarez, M. J.: A Proposal for the Intercomparison of the Dynamical Cores of Atmospheric General Circulation Models, Bulletin of the American Meteorological Society, 75, 1825–1830, https://doi.org/https://doi.org/10.1175/1520-
610 0477(1994)075<1825:APFTIO>2.0.CO;2, 1994.

Herbert, C., Caballero, R., and Bouchet, F.: Atmospheric Bistability and Abrupt Transitions to Superrotation: Wave–Jet Resonance and Hadley Cell Feedbacks, Journal of the Atmospheric Sciences, 77, 31–49, https://doi.org/https://doi.org/10.1175/JAS-D-19-0089.1, 2020.

Huang, H.-P., Weickmann, K. M., and Hsu, C. J.: Trend in Atmospheric Angular Momentum in a Transient Climate Change Simulation with Greenhouse Gas and Aerosol Forcing, Journal of Climate, 14, 1525–1534, https://doi.org/10.1175/1520-
615 0442(2001)014<1525:TIAAMI>2.0.CO;2, 2001.

Landau, L. D.: On the theory of phase transitions, Zh. Eksp. Teor. Fiz., 7, 19–32, https://doi.org/10.1016/B978-0-08-010586-4.50034-1, 1937.

Laraia, A. L. and Schneider, T.: Superrotation in Terrestrial Atmospheres, Journal of the Atmospheric Sciences, 72, 4281–4296, https://doi.org/https://doi.org/10.1175/JAS-D-15-0030.1, 2015.

620 Lenton, T., Rockström, J., Gaffney, O., Rahmstorf, S., Richardson, K., Steffen, W., and Schellnhuber, H.: Climate tipping points — too risky to bet against, Nature, 575, 592–595, https://doi.org/10.1038/d41586-019-03595-0, 2019.

Lenton, T. M.: Early warning of climate tipping points, Nature Climate Change, 1, 201–209, 2011.

Lenton, T. M., Livina, V. N., Dakos, V., van Nes, E. H., and Scheffer, M.: Early warning of climate tipping points from critical slowing down: comparing methods to improve robustness, Phil. Trans. R. Soc. A, 370, 1185–1204, 2012.

625 Livina, V. N. and Lenton, T. M.: A modified method for detecting incipient bifurcations in a dynamical system, Geophys. Res. Lett., 34, L03 712, 2007.

Mann, M. E., Rahmstorf, S., Kornhuber, K., Steinman, B. A., Miller, S. K., and Coumou, D.: Influence of Anthropogenic Climate Change on Planetary Wave Resonance and Extreme Weather Events, Scientific Reports, 7, 45 242, https://doi.org/10.1038/srep45242, 2017.

Mecking, J. V., Drijfhout, S. S., Jackson, L. C., and Graham, T.: Stable AMOC off state in an eddy-permitting coupled climate model, Clim.
630 Dyn., doi:10.1007/s00382-016-2975-0, 1–16, 2016.

Mitchell, J. L. and Vallis, G. K.: The transition to superrotation in terrestrial atmospheres, Journal of Geophysical Research: Planets, 115, https://doi.org/10.1029/2010JE003587, 2010.

Pierrehumbert, R. T.: Climate change and the tropical Pacific: The sleeping dragon wakes, Proceedings of the National Academy of Sciences, 97, 1355–1358, https://doi.org/10.1073/pnas.97.4.1355, 2000.

635 Read, P. L. and Lebonnois, S.: Superrotation on Venus, on Titan, and Elsewhere, Annual Review of Earth and Planetary Sciences, 46, 175–202, https://doi.org/10.1146/annurev-earth-082517-010137, 2018.

Saravanan, R.: Equatorial Superrotation and Maintenance of the General Circulation in Two-Level Models, Journal of the Atmospheric Sciences, 50, 1211–1227, https://doi.org/10.1175/1520-0469(1993)050<1211:ESAMOT>2.0.CO;2, 1993.

Scheffer, M., Bacompte, J., Brock, W. A., Brovkin, V., Carpenter, S. R., Dakos, V., Held, H., van Nes, E. H., Rietkerk, M., and Sugihara, G.:
640 Early warning signals for critical transitions, Nature, 461, 53–59, 2009.

Scheffer, M., Carpenter, S. R., Lenton, T. M., Bascompte, J., Brock, W., Dakos, V., van de Koppel, J., van de Leemput, I. A., Levin, S. A., van Nes, E. H., Pascual, M., and Vandermeer, J.: Anticipating Critical Transitions, Science, 338, 344–348, 2012.

Shell, K. M. and Held, I. M.: Abrupt Transition to Strong Superrotation in an Axisymmetric Model of the Upper Troposphere, Journal of the Atmospheric Sciences, 61, 2928–2935, https://doi.org/10.1175/JAS-3312.1, 2004.

645 Stommel, H.: Thermohaline convection with two stable regimes of flow, Tellus, 13, 224–230, 1961.

Strogatz, S. H.: Nonlinear Dynamics and Chaos, Westview Press, 2001.

Suarez, M. J. and Duffy, D. G.: Terrestrial Superrotation: A Bifurcation of the General Circulation, Journal of the Atmospheric Sciences, 49, 1541–1554, https://doi.org/10.1175/1520-0469(1992)049<1541:TSABOT>2.0.CO;2, 1992.

Tantet, A., van der Burgt, F. R., and Dijkstra, H. A.: An early warning indicator for atmospheric blocking events using transfer operators,
650 Chaos, 25, 2015.

Thompson, J. M. T. and Sieber, J.: Predicting climate tipping as a noisy bifurcation: A review, Int. J. Bif. Chaos, 21, 399–423, 2011.

Tziperman, E. and Farrell, B.: Pliocene equatorial temperature: Lessons from atmospheric superrotation, Paleoceanography, 24, https://doi.org/10.1029/2008PA001652, 2009.

Vallis, G. K., Colyer, G., Geen, R., Gerber, E., Jucker, M., Maher, P., Paterson, A., Pietschnig, M., Penn, J., and Thomson, S. I.: Isca, v1.0:
655   a framework for the global modelling of the atmospheres of Earth and other planets at varying levels of complexity, Geosci. Model Dev.,
11, 843–859, https://doi.org/10.5194/gmd-11-843-2018, 2018.

Vellinga, M. and Wood, R. A.: Global climatic impacts of a collapse of the Atlantic thermohaline circulation, Clim. Change, 54, 43–63, 2002.

von Storch, H. and Zwiers, F. W.: Statistical Analysis in Climate Research, Cambridge University Press, 1999.

Wieczorek, S., Ashwin, P., Luke, C. M., and Cox, P. M.: Excitability in ramped systems: The compost-bomb instability, P. R. Soc. A, 10,
660   1098, 2010.

Wiesenfeld, K.: Noisy precursors of nonlinear instabilities, J. Stat. Phys., 38, 1071–1097, 1985.

Williamson, M. S. and Lenton, T. M.: Detection of bifurcations in noisy coupled systems from multiple time series, Chaos, 25, 036 407,
2015.